Aus dem

Institut für Prophylaxe und Epidemiologie der Kreislaufkrankheiten (IPEK)

Klinikum der Ludwig-Maximilians-Universität München

The regulation of mitochondrial function and lipid droplet formation by Dicer in plaque macrophages

Dissertation
zum Erwerb des Doktorgrades der Medizin
an der Medizinischen Fakultät
der Ludwig-Maximilians-Universität München

vorgelegt von
Nan Li

aus
Henan, China

Jahr
2025

Mit Genehmigung der Medizinischen Fakultät der
Ludwig-Maximilians-Universität München

Erstes Gutachten:	Prof.Dr. Andreas Schober
Zweites Gutachten:	Prof.Dr. Sebastian Kobold
Drittes Gutachten:	Prof. Dr. Heiko Adler

Dekan: Prof. Dr. med. Thomas Gudermann

Tag der mündlichen Prüfung: 20.November 2025

Table of contents

Zusammenfassung (Deutsch)

Hintergrund:

Die Expansion des nekrotischen Kerns ist ein wesentlicher Faktor für das Fortschreiten atherosklerotischer Plaques und erhöht das Risiko einer Plaqueruptur sowie thrombotischer Ereignisse, wie Myokardinfarkt und Schlaganfall. Die Bildung von Cholesterinkristallen spielt eine zentrale Rolle bei der Entwicklung des nekrotischen Kerns und steht im Zusammenhang mit der sekundären Nekrose von Lipidtröpfchen (LD)-haltigen Plaque-Makrophagen. Die zugrunde liegenden molekularen Mechanismen sind bislang jedoch nur unzureichend verstanden. Dicer ist eine Schlüssel-Endonuklease in der Biogenese von microRNAs. Unsere vorhergehenden Studien deuten darauf hin, dass die Dicer-Expression in Makrophagen die Lipidakkumulation, Apoptose und die Bildung des nekrotischen Kerns in atherosklerotischen Plaques begrenzt. In vitro fördert Dicer die mitochondriale Atmung in LD-haltigen Makrophagen. Ob Dicer jedoch auch in vivo die mitochondriale Funktion in Plaque-Makrophagen reguliert, ist bislang unklar. Ziel dieser Studie war es daher zu untersuchen, ob Dicer durch die Förderung der mitochondrialen Funktion die Lipidakkumulation in Plaque-Makrophagen reduziert und damit Apoptose, sekundäre Nekrose und Cholesterinkristallbildung begrenzt. Zudem wurde geprüft, ob diese Effekte durch microRNAs vermittelt werden.

Methoden:

Es wurde ein konfokaler Live-Imaging-Ansatz zur Analyse der Funktion von Dicer in Makrophagen atherosklerotischer Plaques unter Verwendung von Aortenbogen- bzw. Aortenwurzelgewebe von $Apoe^{-/-}$mTmG/$LysMCre^{T/T}$/$Dicer^{flox/flox}$ und $Apoe^{-/-}$mTmG/$LysMCre^{T/T}$/$Dicer^{WT/WT}$ Mäusen nach 12 bzw. 24 Wochen fettreicher Diät etabliert. Die Cholesterinkristallbildung wurde mittels Polarisations- und konfokaler Reflexionsmikroskopie erfasst. Die mitochondriale Atmung im lebenden Plaquegewebe wurde durch Seahorse-Analysen bestimmt. Zusätzlich führten wir GFP-RIP-Seq, Proteomik und ein NanoString-MicroRNA-Profiling durch, um Dicer-vermittelte microRNAs und deren Zielgene zu identifizieren.

Ergebnisse:

Es wurden drei Makrophagensubtypen innerhalb der atherosklerotischen Plaques, basierend auf dem Gehalt an LDs und der mitochondrialen gefunden: LD^{high} (>20% LDs), LD^{inter} (5-20% LDs) und LD^{low} (<5% LDs) Makrophagen. LD^{high}-Makrophagen zeigten eine verringerte mitochondriale Aktivität im Vergleich zu LD^{inter} und LD^{low},

was primär auf ein erhöhtes Protonen-leack zurückzuführen war. Dicer begrenzte die Entstehung von LD^{high}-Makrophagen durch die Hemmung der Bildung von Mitochondrien, die mit LDs assoziiert sind, sogenannte „peridroplet mitochondria“ (PDM), sowie die LD-Expansion. Zudem reduzierte Dicer die mitochondriale Dysfunktion in Plaque-Makrophagen, wodurch die Freisetzung von mtDNA und die Typ-I-Interferonantworten eingeschränkt wurden. In der Folge senkte Dicer die Caspase-3-Aktivierung in LD^{high}-Makrophagen und verhinderte so sekundäre Nekrose. Bemerkenswerterweise wurden Cholesterinkristalle bevorzugt an der Grenzfläche extrazellulärer DNA-Ablagerungen beobachtet. Durch die Vermeidung der DNA-Freisetzung aus sekundär nekrotischen Zellen schränkte Dicer die Cholesterinkristallbildung ein. Mechanistisch konnten Ftl1 und Vim als Zielgene der Dicer-regulierten miR-22-3p bzw. miR-30d-5p identifiziert werden, welche an der Regulation der mitochondrialen Funktion und PDM-Dynamik beteiligt sein könnten.

Schlussfolgerung:

Diese Studie stellt eine neuartige konfokale Bildgebungsmethode zur Echtzeit-Analyse von Makrophagenfunktionen in lebenden atherosklerotischen Plaques vor. Erstmals liefern wir in vivo Evidenz für die Existenz von PDM in Plaque-Makrophagen und zeigen deren Rolle bei der LD-Expansion auf. Zudem identifizieren wir extrazelluläre DNA als zentralen Faktor bei der Cholesterinkristallbildung. Darüber hinaus belegen wir, dass Dicer eine entscheidende Schutzfunktion gegenüber der durch Cholesterinkristalle induzierten Bildung eines nekrotischen Kerns ausübt, indem es die mitochondriale Funktion erhält und die LD-Expansion in LD^{high}-Makrophagen einschränkt. Diese protektive Wirkung könnte über die miR-22-Ftl1- und miR-30-Vim-Achsen vermittelt werden, welche mit der Regulation der mitochondrialen Funktion über Eisenhomöostase bzw. Zytoskelettumbau in Verbindung stehen. Auch wenn diese Signalwege weiterer Untersuchung bedürfen, stellen sie potenzielle Zielstrukturen für therapeutische Interventionen dar, mit dem Ziel, die mitochondriale Funktion von Plaque-Makrophagen zu verbessern und den nekrotisch bedingten Fortschritt der Atherosklerose einzudämmen.

Abstract (English)

Background:

Expansion of the necrotic core is a major contributor to plaque progression in atherosclerosis, increasing the risk of plaque rupture and thrombotic events such as myocardial infarction and stroke. Cholesterol crystal (CC) formation plays a critical role in necrotic core development and has been linked to secondary necrosis of LD-containing plaque macrophages. However, the molecular mechanisms governing this process remain poorly understood. Dicer is a key endonuclease in microRNA biogenesis. Our previous study suggests that Dicer expression in macrophages limits macrophage lipid accumulation, apoptosis, and necrotic core formation in atherosclerotic plaques. In vitro, Dicer enhances mitochondrial respiration in LD-containing macrophages. However, the role of Dicer in regulating mitochondrial function in plaque macrophages in vivo remains unknown. This study aimed to determine whether Dicer reduces lipid accumulation by enhancing mitochondrial respiration in live plaque macrophages, thereby limiting apoptosis, secondary necrosis, and CC formation. Furthermore, this study aimed to determine whether Dicer-dependent microRNAs mediate these effects.

Methods:

A live plaque confocal imaging approach was established to investigate the role of Dicer in macrophages in atherosclerotic plaques, using aortic arch or root tissue from the $Apoe^{-/-}$mTmG/$LysMCre^{T/T}$/$Dicer^{flox/flox}$ and $Apoe^{-/-}$mTmG/$LysMCre^{T/T}$/$Dicer^{WT/WT}$ mice after 12 or 24 weeks of high-fat diet feeding. CC formation was detected by polarized microscopy and confocal reflection microscopy. Mitochondrial respiration in live plaque tissue was measured using a Seahorse assay. Furthermore, I performed GFP-tagged Ago2-RIP-seq, proteomics, and NanoString microRNA profiling to identify Dicer-mediated miRNAs and their targets.

Results:

Three macrophage subtypes within atherosclerotic plaques were identified based on lipid droplet (LD) content: LD^{high}, LD^{inter}, and LD^{low} macrophages. LD^{high} macrophages showed reduced mitochondrial activity compared to LD^{low} macrophages, primarily due to increased proton leak. Dicer restricted LD^{high} macrophage formation by suppressing peri-droplet mitochondria (PDM) formation and LD expansion. In addition, Dicer limited mitochondrial dysfunction in plaque macrophages, thus

limiting mtDNA release and Type I interferon responses. Consequently, Dicer reduced caspase-3 activation in LD^{high} macrophages, thereby limiting secondary necrosis. Notably, CCs were observed to form at the interface of extracellular DNA deposits. By preventing extracellular DNA deposition from secondary necrotic cells, Dicer restricted CC formation. Mechanistically, Ftl1 and Vim, identified as targets of Dicer-mediated miR-22-3p and miR-30d-5p, respectively, may be involved in regulating mitochondrial function and PDM dynamics.

Conclusion:

This study provides a novel confocal imaging method for real-time functional analysis of macrophages in live atherosclerotic plaques. Using this approach, this study presents the first in vivo evidence of PDM in plaque macrophages and reveal their role in LD expansion. This study also offers new insight into CC formation, highlighting its association with extracellular DNA deposition. Furthermore, this study demonstrates that Dicer plays a critical role in restraining CC-driven necrotic core expansion by preserving mitochondrial function and limiting LD expansion in LD^{high} macrophages. This protective effect may involve the Dicer-regulated miR-22-Ftl1 and miR-30-Vim axes, which have been implicated in regulating mitochondrial function through iron homeostasis and cytoskeletal remodeling, respectively. While these pathways require further investigation, they represent promising targets for therapeutic intervention aimed at improving mitochondrial function of plaque macrophages to prevent necrotic core-driven atherosclerotic progression.

List of Figures

List of abbreviations

3’ UTR	3’ untranslated region
ABCA1	ATP-Binding Cassette Transporter A1
Ago	Argonaute
Akt1	AKT Serine/Threonine Kinase 1
Arntl	aryl hydrocarbon receptor nuclear translocator-like
BCL6	B cell CLL/lymphoma 6
BMDMs	Bone Marrow-Derived Macrophages
C3	Complement Component 3
C3D	Caspase 3 activated DNA dye
CC	cholesterol crystal
CD36	cluster of differentiation 36
CD74	Cluster of Differentiation 74
Cd9	Cluster of Differentiation 9
Ctsb	Cathepsin B
DECR1	2,4-Dienoyl-CoA Reductase 1
DEP	differentially expressed proteins
dsRBD	double-stranded RNA-binding domain
EC	endothelial cell
ER	Endoplasmic Reticulum
FAO	Fatty Acid Oxidation
FC	fold change
FCCP	Carbonyl Cyanide-p-Trifluoromethoxyphenylhydrazone
FOXO3	Forkhead Box O3
Ftl1	Ferritin Light Chain 1
GFP	Green Fluorescent Protein
HBP1	HMG-Box Transcription Factor 1
Hsp90ab1	Heat Shock Protein 90 Alpha Family Class B Member 1
IFIT3	Interferon-Induced Protein With Tetratricopeptide Repeats 3
IFN-γ	interferon-gamma
IFNIC	interferon-inducible cell
IL-10	Interleukin-10
IL-12	Interleukin-12
IL-13	Interleukin-13
IL-1β	Interleukin-1 Beta

IPA	Ingenuity Pathway Analysis
ISG15	Interferon-Stimulated Gene 15
KLF4	Krüppel-Like Factor 4
LC-MS/MS	liquid chromatography-tandem mass spectrometry
Lcor	Ligand Dependent Nuclear Receptor Corepressor
LD	lipid droplet
LDL	low-density lipoprotein
Lgals3	advanced glycation end-product receptor 3
Lpl	Lipoprotein Lipase
LPS	lipopolysaccharide
LysM	M-lysozyme
Mac2	Macrophage Antigen 2
MAC^{AIR}	Aortic intima resident macrophages
miRNA	microRNA
Mmp12	Matrix Metallopeptidase 12
MOMP	mitochondrial outer membrane permeabilization
mtDNA	Mitochondrial DNA
mTmG	Membrane Tomato-membrane GFP
NF-κB	Nuclear Factor Kappa-Light-Chain-Enhancer of Activated B Cells
NLRP3	NLR Family Pyrin Domain Containing 3
OCR	Oxygen Consumption Rate
oxLDL	oxidized low-density lipoprotein
PAZ	PIWI-Argonaute-Zwille Domain
PDM	peri-droplet mitochondria
PLIN2	Perilipin 2
RIP	RNA Immunoprecipitation
RISC	RNA-induced silencing complex
RNAi	RNA interference
SOCS1	Suppressor of Cytokine Signaling 1
SPP1	Secreted Phosphoprotein 1
SR-A1	Scavenger Receptor Class A Member 1
SRC	Spare Respiratory Capacity
STAT1	Signal Transducer and Activator of Transcription 1
STAT2	Signal Transducer and Activator of Transcription 2
TAG	Triacylglycerol
tAGO2	Tagged Argonaute 2

TFEB	Transcription Factor EB
TLF	Timd4, Lyve1, Folr2
Trem2	Triggering Receptor Expressed on Myeloid Cells 2
Vim	Vimentin
Xaf1	XIAP-Associated Factor 1

1. Introduction

1. 1 Pathogenesis of atherosclerosis

Cardiovascular diseases remain the leading cause of morbidity and mortality worldwide[1]. Atherosclerosis, the primary pathological basis of cardiovascular diseases, is a chronic inflammatory condition characterized by the buildup of lipids and immune cells in the sub-endothelium of the arterial wall. In the initial stage of atherosclerosis, risk factors such as high cholesterol, hypertension, obesity, diabetes, smoking, and low-shear stress[2-5] trigger the increase in the endothelial permeability and the retention of cholesterol-rich lipoproteins, primarily low-density lipoprotein (LDL), in the sub-endothelial space. The trapped LDL particles are susceptible to oxidative modification, resulting in oxidized LDL (oxLDL), which initiates an inflammatory process and activates endothelial cells (ECs). Activated ECs express adhesion molecules that attract circulating monocytes to the intima surface. Monocytes then enter the intima and differentiate into macrophages in response to cytokines and the macrophage colony-stimulating factor. In atherosclerotic lesions, macrophages take up oxLDL through scavenger receptors like CD36 and SR-A1[6]. Subsequently, oxLDL is processed in the endolysosome, where lysosomal acid lipase hydrolyzes the cholesterol ester to free cholesterol[7]. Excessive accumulation of free cholesterol stimulates its re-esterification by acyl-coenzyme A: cholesterol acyltransferase-1 in the endoplasmic reticulum (ER), leading to the storage of cholesterol ester in lipid droplets (LDs). Conversely, cholesterol ester can be converted again to free cholesterol by the action of cholesteryl ester hydrolase. Moreover, free cholesterol can be removed from the macrophages via the reverse cholesterol transport pathway involving high-density lipoprotein and cholesterol transporters, such as ABCA1[8,9]. During atherosclerosis progression, excessive uptake of oxLDL leads to LD-containing macrophage (foam cell) formation (Fig. 1). Although macrophages also take up native LDL via the LDL receptor, this pathway does not lead to foam cell formation. Lipid and foam cell accumulation drives the formation of plaques, the hallmark of atherosclerosis[10]. The lipid overload induces loss of membrane fluidity[11,12], ER stress[13], mitochondrial dysfunction[14], intracellular cholesterol crystallization[12], and oxysterol formation[15]. These pathological processes ultimately cause apoptotic cell death (Fig. 1), contributing to plaque necrotic core formation. The growth of atherosclerotic plaques results in vascular stenosis and luminal occlusion[16]. Furthermore, large necrotic cores heighten the plaque's vulnerability to rupture, thereby inducing atherothrombosis and ultimately leading to ischemic cardiovascular diseases such as myocardial infarction and stroke[16,17].

Thus, reducing the size of the necrotic core presents a promising therapeutic strategy to mitigate the consequences of atherosclerosis.

1.2 Necrotic core formation in atherosclerosis

The necrotic core mainly consists of cell debris and CC[16]. Secondary necrosis, referring to the necrosis of apoptotic cells that are not efficiently cleared, is a key contributor to necrotic core formation (Fig. 1)[17]. Chronic inflammation and excess lipid accumulation induce plaque cell apoptosis, primarily in macrophages, probably caused by ER stress and mitochondrial dysfunction[18-21]. In early-stage plaques, apoptotic cells were efficiently removed by neighboring macrophages through the process known as efferocytosis[22]. This process limits inflammation by preventing inflammatory content release from apoptotic cells and triggering the release of anti-inflammatory factors like IL-10[23]. However, this apoptosis-efferocytosis balance is disrupted in the advanced plaque due to increased apoptosis and defective efferocytosis (Fig. 1)[22]. Notably, circadian rhythm-regulated microRNAs (miRNAs) have been shown to promote apoptosis to a degree that exceeds the compensatory capacity of efferocytosis, thereby contributing to necrotic core formation[24]. This suggests a more dominant role for apoptosis in driving the imbalance and subsequent necrotic core formation.

CC is another major necrotic core component associated with plaque vulnerability (Fig. 1)[25]. Although the mechanisms of CC formation in the plaque are poorly understood, this process has been linked to secondary necrosis (Fig. 1) and high levels of free cholesterol accumulation, either intracellularly or spontaneously in the extracellular space within the necrotic core[25-27]. Intracellular CC formation induces several pathological processes, including NLRP3 inflammasome formation and subsequent inflammatory activation, plasma membrane damage, lysosome rupture, and apoptosis[25]. Extracellular CC growth in the necrotic core is associated with plaque rupture and thrombosis[28], e.g., by puncturing the intima[29].

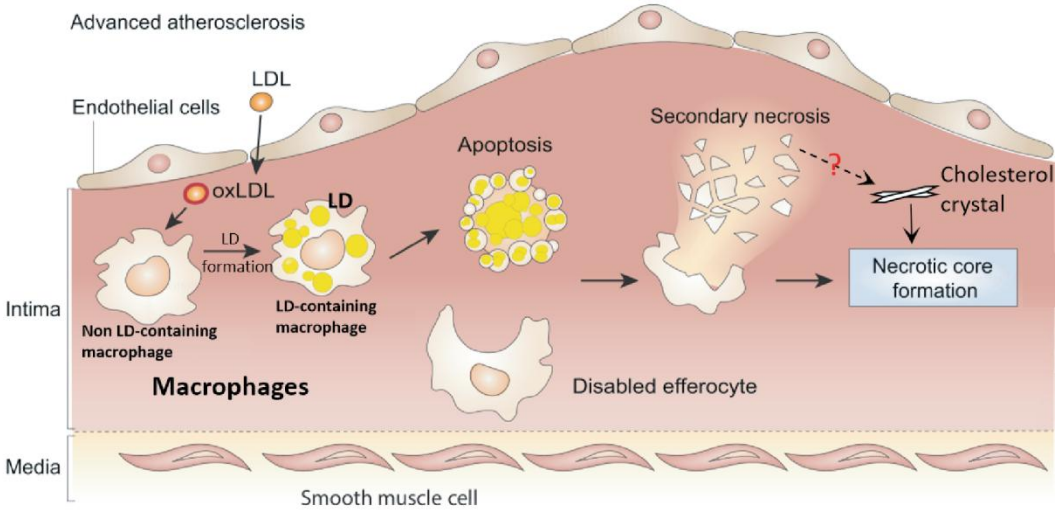

Fig. 1: Role of macrophages in necrotic core formation

In advanced atherosclerotic lesions, LDL infiltrates the intima and becomes oxidized, resulting in oxLDL accumulation, which is taken up by macrophages, leading to LD formation. Macrophages containing LDs undergo apoptosis due to lipid overload conditions. In the absence of efficient efferocytosis, apoptotic cells progress to secondary necrosis, releasing intracellular contents and cell debris that contribute to necrotic core formation. Secondary necrosis is also related to CC deposition, another key component of the necrotic core, although the underlying mechanism is poorly understood. The figure is adapted from[22].

1.3 Macrophage subtypes in atherosclerosis

Macrophages demonstrate exceptional plasticity, enabling them to alter their functional phenotype in adaptation to distinct stimuli. In atherosclerotic plaques, most macrophages accumulate lipids and transform into foam cells. In addition, both pro-inflammatory and anti-inflammatory macrophages have been described within the lesion. Pro-inflammatory macrophages produce cytokines like IL-1β and IL-12, and attract monocytes through chemokines such as monocyte chemoattractant protein-1. Conversely, anti-inflammatory macrophages play an anti-inflammatory role by producing pro-resolving cytokines like IL-10[30]. While pro-inflammatory macrophages are more abundant during the progression of atherosclerosis, and are enriched in the rupture-prone shoulder region of the plaque, anti-inflammatory macrophages play a prominent role during the regression of atherosclerosis, and are the predominant population in the adventitia[31,32]. To investigate macrophage subtype function in vitro, resting macrophages are polarized into pro-inflammatory phenotype (M1 macrophage) upon lipopolysaccharide (LPS) and interferon-gamma (IFN-γ) stimulation, and into anti-inflammatory phenotype (M2 macrophage) in

response to interleukin (IL)-4 and/or IL-13[33]. Moreover, foam cell formation is induced by treating macrophages with oxLDL. Nevertheless, M1/M2 polarized macrophages and oxLDL-induced foam cells are defined under pure and idealized conditions. Their relevance to in vivo macrophages, which are exposed to a much more complex microenvironment, remains uncertain.

Recent single cell sequencing studies reveal macrophage heterogeneity in atherosclerosis. In mice and humans, macrophages are primarily classified into four subgroups: inflammatory-M Φ macrophages, resident-like macrophages (TLF resident macrophage and aorta intima resident macrophage), Trem2^{+} foam macrophages, and interferon-inducible cell (IFNIC) macrophages (Fig. 2)[34-39]. Resident-like macrophages expressed increased anti-inflammatory mRNA markers[37], while inflammatory-M Φ macrophages and IFNIC macrophages showed enrichment of inflammatory markers[34,40]. Meanwhile, Trem2^{+} foam cells express mRNAs involved in cholesterol metabolism and oxidative phosphorylation[37]. Although these macrophage subtypes in vivo share some similarities with in vitro cell models, they do not fully correspond to in vitro-defined subtypes and show less distinct boundaries, with partial transcriptional and functional overlap. MAC^{AIR} macrophages show pro-inflammatory mRNA expression of IL-1β. However, they also shared an expression pattern with Trem2^{+} foam cells, including Mmp12, Lgals3, Cd9, and Lpl, highlighting their functional complexity. Notably, these major macrophage subtypes represent a shared subset identified across multiple single-cell sequencing studies. However, the complete spectrum of macrophage phenotypes varies across studies due to methodological differences, sample origin, pathological phase, and species. This highlights the heterogeneity of macrophage populations in atherosclerosis. Therefore, the applicability of in vitro macrophage phenotype classification to atherosclerotic lesions is challenged. Additionally, although the mRNA expression patterns of macrophage subtypes in vivo have been identified, further functional investigation is required to elucidate their roles in atherosclerosis.

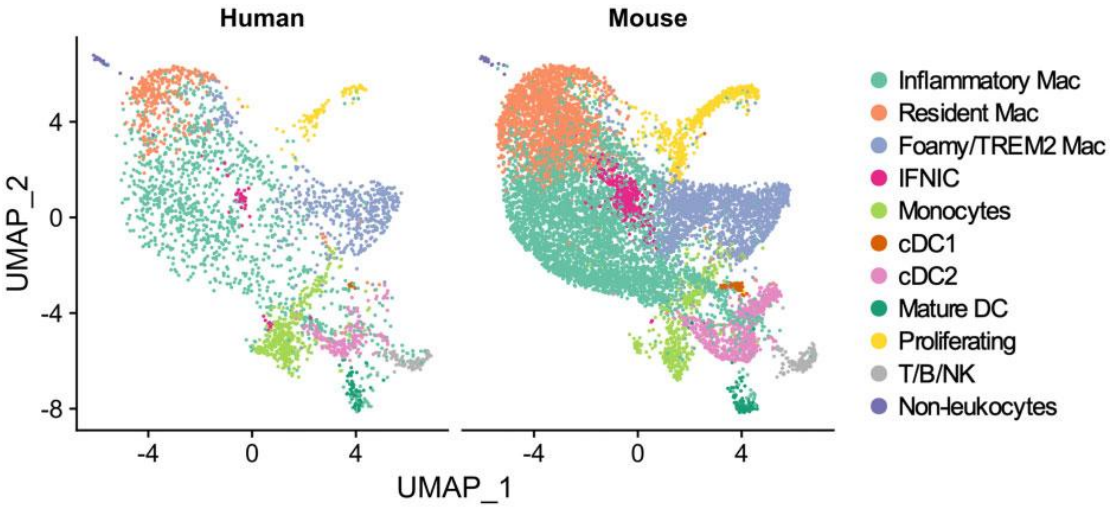

Fig. 2: Myeloid cell populations in human and mouse atherosclerotic lesions

Uniform Manifold Approximation and Projection (UMAP) plots showing the clustering of single-cell RNA sequencing (scRNA-seq) data from human (left) and mouse (right) atherosclerotic arteries. Both species share distinct macrophage subsets, including inflammatory, resident, foamy/TREM2+, and interferon-inducible (IFNICs). In addition, myeloid populations include monocytes, conventional dendritic cells (cDC1 and cDC2), mature DCs, and a minor fraction of proliferating cells, lymphocytes, and non-leukocytic cells. Data were integrated across multiple datasets and visualized in a species-separated manner for cross-species comparison. Figure is adapted from[35].

1.4 Role of Dicer and miRNAs in atherosclerosis

1.4.1 Function of Dicer and miRNAs

RNase III Dicer is a key regulator of the RNA interference (RNAi) pathway, controlling the production of miRNA and several other small RNAs. In the canonical miRNA biogenesis process, the PAZ and platform domains from the head region of Dicer recognize and bind to the 3′ overhang and the 5′ phosphate of one strand of the double-stranded pre-miRNA substrate, respectively (Fig. 3)[41,42]. Additionally, the helicase, dsRBD and DUF283 domains also functions in substrate recognition through RNA binding (Fig. 3)[43-45]. Next, RNase IIIa and IIIb domains in the body region each cleave one strand from the double-strand pre-miRNA[46] near the terminal hairpin loop (Fig. 3) to generate the ~22 nt miRNA duplex [47].

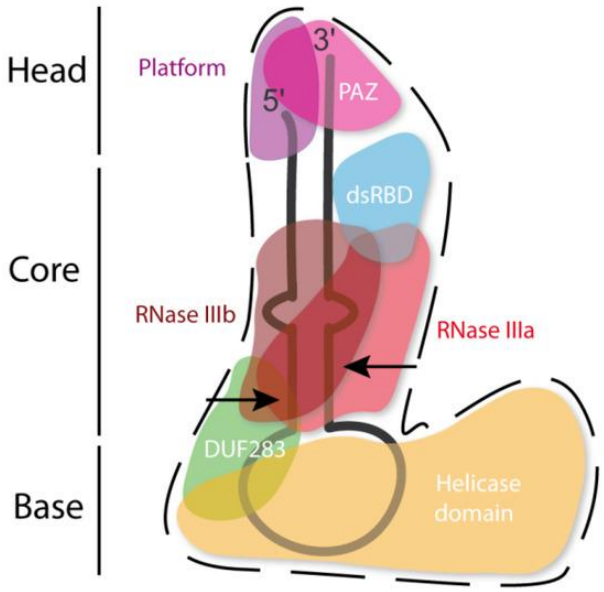

Fig. 3: Structural organization of the Dicer protein

The Dicer protein shows an "L" shape, containing distinct structural domains that coordinate RNA recognition and processing. The head region contains the platform and PAZ domains, which bind the 5' phosphate and 3' two nucleotides overhang of pre-miRNA substrates, respectively. The core region includes a double-stranded RNA-binding domain (dsRBD) and two RNase III domains (RNase IIIa and RNase IIIb), responsible for cleaving the double-stranded RNA to generate mature miRNAs. The base region comprises the helicase domain and DUF283 domain, which are implicated in RNA binding, unwinding, and substrate positioning. Together, these domains enable Dicer to cleave pre-miRNAs with precise length specificity. The figure was adapted from[48].

The miRNA duplex is subsequently loaded onto the Argonaute (AGO) protein by Dicer with the assistance of TAR RNA-binding protein (TRBP). TRBP facilitates correct strand selection by sensing duplex asymmetry and orienting the RNA appropriately for AGO loading. Prior to loading, unloaded AGO proteins are maintained in an open conformation by the HSP90 dimer and its co-chaperones, allowing efficient duplex accommodation. Upon loading, AGO proteins cleave the passenger strand and retain the guide strand, leading to the assembly of the mature RNA-induced silencing complex (RISC, Fig. 4)[49-51].

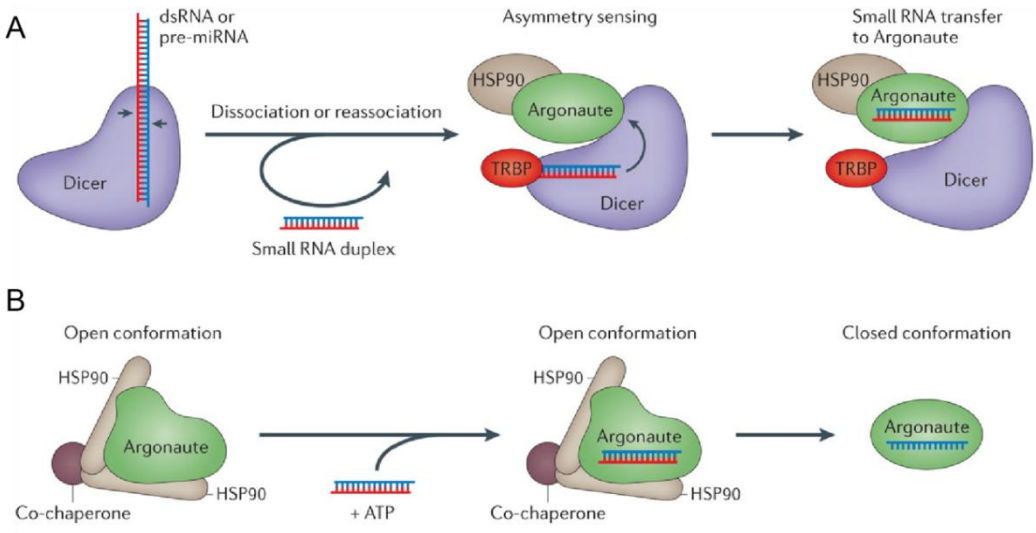

Fig. 4: Loading of miRNAs onto AGO protein

(A) Dicer processes long dsRNAs or pre-miRNAs into ~21 nt RNA duplexes via its two RNase III domains (arrows). The duplex transiently dissociates and reassociates to Dicer, where TRBP detects strand asymmetry and positions the duplex to ensure correct guide strand selection. The RNA is then transferred to AGO, which is held in an open conformation by HSP90. (B) HSP90 dimers, together with co-chaperones, maintain unloaded AGO proteins in an open conformation. Following RNA duplex binding, the passenger strand (red) is removed, HSP90 hydrolyzes ATP, and AGO undergoes a conformational shift to the closed state , retaining the guide strand (blue). Subsequently, HSP90 and its co-chaperones dissociate from the complex. The figure was adapted from[51].

RISC functions in gene silencing at the post-transcriptional level by targeting mRNA. Recognition of target mRNA was based on the Watson-Crick base-pairing between the 3' untranslated region (3' UTR) binding sites of the target mRNA and the miRNA seed sequence[52]. This base-pairing leads to translational repression or target mRNA decay [53,54]. Apart from its canonical role in miRNA maturation, Dicer has been reported to play a role in non-canonical nuclear RNA interference pathway[55-57], DNA damage response, and dsRNA removal[58,59].

1.4.2 Role of macrophage miRNAs in atherosclerosis

Macrophage miRNAs play crucial roles in regulating atherosclerosis. In foam cells, multiple miRNAs, including miR-27a/b, miR-19b, miR-144-3p, miR-758, miR-33-3p/-5p, and miR-378[60], target ABCA1, a cholesterol transporter, thereby affecting cholesterol efflux and lipid accumulation. Notably, miR-33 has also been shown to disrupt lipophagy-associated lipid metabolism through targeting FOXO3

and TFEB[61]. Moreover, oxLDL induces miR-155 expression, which enhances lipid accumulation in macrophages through repression of HBP1[62].

In addition to lipid metabolism, miRNAs are also critical regulators of inflammation in atherosclerosis. The expression of miR-155 is elevated in atherosclerotic lesions and inflammatory cells, where it enhances NF-κB activation and the subsequent inflammatory response by targeting aryl hydrocarbon receptor nuclear translocator-like (Arntl), SOCS1, and B cell CLL/lymphoma 6 (BCL6)[47]. Notably, another highly up-regulated miRNA in lesional macrophages, miR-342-5p, promotes miR-155 expression and inflammation by targeting Akt1 in inflammatory macrophages[63].

Additionally, miRNAs regulate necrotic core formation by influencing cell death. Macrophage miR-21 shows a circadian expression pattern and contributes to the diurnal regulation of apoptosis in atherosclerotic plaques by targeting Xaf1[24]. In inflammatory macrophages, miR-383 reduces ATP consumption by targeting Parg and prevents necroptosis[64].

Moreover, mitochondrial respiration represents another pathway through which miRNAs influence macrophage viability. Expression of miR-10 in macrophages regulates FAO-fueled mitochondrial respiration by targeting Lcor, thereby limiting lipid accumulation and apoptosis in macrophages[65]. Similarly, miR-210 restricts FAO-dependent mitochondrial respiration by targeting DECR1, thus promoting necroptosis[64].

1.4.3 Role of Dicer in atherosclerosis

Global loss of Dicer in mice leads to embryonic lethality[66], suggesting the essential role of Dicer-mediated miRNA production in mouse development. Deletion of Dicer, specifically in macrophages or ECs of $Apoe^{-/-}$ mice, decreases the expression of many miRNAs[65,67]. However, the effect of Dicer depletion on atherosclerosis is opposite between macrophages and ECs. In contrast to EC, where Dicer promotes atherosclerosis via miR-103-mediated suppression of KLF4, Dicer expression in macrophages decreases plaque macrophage apoptosis and necrotic core formation. This effect of Dicer in macrophages is likely mediated by miR-10a, a Dicer-regulated miRNA that targets Lcor, thereby enhancing FAO-fueled mitochondrial respiration and limiting lipid accumulation, as demonstrated in bone marrow-derived macrophages (BMDMs)[65]. However, the mechanistic link between Dicer-regulated mitochondrial respiration, lipid accumulation, and macrophage apoptosis in vivo remains poorly understood. Given the macrophage heterogeneity in vitro and in vivo,

how Dicer regulates distinct macrophage subtypes in plaques and thereby contributes to atherosclerosis is not fully elucidated.

1.5 Hypothesis and Aims

The size of the necrotic core determines the vulnerability of plaques to rupture, which can lead to arterial obstruction. A primary component of the necrotic core is CCs, which may also contribute to its expansion, along with the secondary necrosis of macrophages. However, it remains unclear how crystal formation in the necrotic core is regulated. Previous research has demonstrated that macrophage Dicer expression reduces lipid accumulation and apoptosis of plaque macrophages, thereby limiting necrotic core formation. Additionally, Dicer enhances mitochondrial respiration in LD-containing macrophages in vitro. Based on these findings, the hypothesis of this study is that Dicer reduces lipid accumulation in LD-containing plaque macrophages by enhancing mitochondrial respiration by generating miRNAs, thereby preventing apoptosis and secondary necrosis. These effects of Dicer limit necrotic core expansion driven by CC formation.

To test this hypothesis, the following aims were addressed:

First, this study evaluated whether Dicer limits lipid accumulation of LD-containing plaque macrophages by enhancing mitochondrial function. To this end, a live plaque imaging approach was established utilizing reporter mice and confocal microscopy. Additionally, mitochondrial respiration in live plaque tissue was assessed using the Seahorse assay.

Second, the effect of Dicer on apoptosis and secondary necrosis of plaque macrophages was examined through live plaque imaging.

Third, this study investigated how secondary necrotic cells contribute to CC formation and whether Dicer modulates this process by combining live plaque imaging with reflection confocal microscopy.

Fourth, the mechanism by which microRNAs mediate the protective role of Dicer in limiting necrotic core formation was explored. For this purpose, GFP-RIP-sequencing was performed in tAGO2 mice, complemented by proteomic analysis and NanoString microRNA profiling in BMDMs.

2.Materials and Methods

2.1 Equipment and software

Equipment	Company
Leica TCS SP8 STED 3X confocal microscope	Leica Microsystem, Germany
DM 6B upright thunder microscope	Leica Microsystem, Germany
Seahorse XFe24 Analyzer	Agilent Technologies, USA
Implen NP80-Touch Spectrophotometer	Implen GmbH, Germany
TissueLyser LT	Qiagen, Germany
Automated capillary-based western blotting system (JESS)	ProteinSimple, USA
QuantStudio™ 6 Flex Real-Time PCR System	Qiagen, Germany
Leica Application Suite (LAS) X version 3.7.5 imaging software	Leica Microsystem, Germany
Fiji (ImageJ, version 2.3.0)	NIH, USA
Prism (Version 10)	GraphPad Software, USA

2.2 Consumables and solutions

REAGENT or RESOURCE	**SOURSE**	**IDENTIFIER**
µ-Slide 4 Well Glass Bottom	ibidi GmbH, Germany	80427
BioTracker NucView® 405 Caspase-3	Sigma-Aldrich, USA	SCT104
BioTracker 405 Blue Mitochondria	Sigma-Aldrich, USA	SCT135
LipidSpot™ 610	Biotium, Inc., USA	70069
MitoView™ 633	Biotium, Inc., USA	70055
MitoTrackerTM Deep Red FM	Thermo Fisher Scientific, USA	M22426
Human Dil high oxidized LDL	Kalen Biomedical, LLC, USA	770262-9
Seahorse XF Calibrant Solution	Agilent Technologies, Inc., USA	100840-000
Seahorse XFe24 Islet Capture FluxPak	Agilent Technologies, Inc., USA	103518-100
Seahorse XF DMEM medium	Agilent Technologies,	103575-100

	Inc., USA	
Seahorse XF 100 mM pyruvate solution	Agilent Technologies, Inc., USA	103578-100
Seahorse XF 1.0 M glucose solution	Agilent Technologies, Inc., USA	103577-100
Seahorse XF 200 mM glutamine solution	Agilent Technologies, Inc., USA	103579-100
Oligomycin A	Sigma-Aldrich, USA	579-13-5
FCCP	Sigma-Aldrich, USA	370-86-5
Rotenone	Sigma-Aldrich, USA	83-79-4
Antimycin A	Sigma-Aldrich, USA	1397-94-0
Jess 12-230 kDa Separation Module, 8 x 25 capillary cartridges	ProteinSimple, USA	SM-W004
Human low-density lipoproteins	ChromoTek GmbH, Germany	437644
D-tube Midi Dialyzer tubes	Merck, Germany	71507-3
Copper(II) sulfate pentahydrate	Sigma-Aldrich, USA	7758-99-8
EDTA	Invitrogen, Thermo Fisher Scientific, USA	AM9260G
PD-10 desalting column	Cytiva, USA	17-0851-01
Lipopolysaccharide	Merck, Germany	L5293
Recombinant Murine IFN-γ	PeproTech, Inc., USA	AF-315-05
GFP-Trap Agarose Kit	ChromoTek, Germany	gtak-20
PicoPure RNA Isolation Kit	Thermo Fisher Scientific, USA	KIT0204
DC protein assay kit	Bio-Rad Laboratories, USA	5000112
12-230 kDa Fluorescence Separation Module, 8 x 25 capillary cartridges	ProteinSimple, USA	SM-FL004
Protein Normalization Module	ProteinSimple, USA	DM-PN02
GFP Antibody (Polyclonal, Rabbit)	Rockland, USA	600-401-215L
Phospho-STAT1 (Tyr701) Monoclonal Antibody (15H13L67)	Invitrogen, USA	701048
Anti-Rabbit IgG-HRP Conjugated Antibody	Bio-Techne, USA	HAF008
Goat Anti-Rabbit Secondary HRP Conjugate	ProteinSimple, USA	042-206

Goat Anti-Mouse Secondary HRP Conjugate	ProteinSimple, USA	040-655
Streptavidin-HRP Conjugate	Bio-Techne, USA	DY998
SuperSignal™ West Pico PLUS Substrate	Thermo Fisher Scientific, USA	34079
Mitochondria Isolation Kit for Cultured Cells	Thermo Fisher Scientific, USA	89874
DNeasy Blood & Tissue Kit	Qiagen, Germany	69504
GoTaq® qPCR and RT-qPCR Systems	Promega, USA	A6001
NucleoSpin miRNA extraction	Machery Nagel, Germany	740971.250
High-Capacity cDNA Reverse Transcription	Applied Biosystems, Germany	4368814
miRCURY LNA RT Kit	Qiagen, Germany	339340
miRCURY Probe PCR Kit	Qiagen, Germany	339371
FTL (Ferritin Light Chain) Polyclonal Antibody	Proteintech, USA	10727-1-AP
Donkey Anti-Rat IgG (H+L), FITC-conjugated	Jackson ImmunoResearch, USA	712-095-153
MAC2 (Galectin-3) Antibody	In-house preparation; Supernatant from hybridoma cell line M3/38.1.2.8 HL.2	
Cy3 AffiniPure Goat Anti-Rabbit IgG (H+L)	Jackson ImmunoResearch, USA	111-165-003
VECTASHIELD® Antifade Mounting Medium with DAPI	Vector Laboratories, USA	H-1200-10

2.3 Mouse Models

$Apoe^{-/-}$ mice expressing Cre recombinase under control of myeloid cell-specific M-lysozyme (Lyz) promoter ($Apoe^{-/-}$LysMCre) were crossed with Dicer floxed mice to generate $Apoe^{-/-}/LysMCre^{T/T}/Dicer^{flox/flox}$ mice[68]. $Apoe^{-/-}/LysMCre^{T/T}/Dicer^{WT/WT}$ mice were used as controls. To generate fluorescent cre reporter mice, $Apoe^{-/-}/LysMCre^{T/T}/Dicer^{flox/flox}$ mice were crossed with mTmG reporter mice[69] (Strain #:007676, The Jackson Laboratory) to obtain $Apoe^{-/-}$mTmG/$LysMCre^{T/T}/Dicer^{flox/flox}$ mice (Fig. 5). $Apoe^{-/-}$mTmG/$LysMCre^{T/T}/Dicer^{WT/WT}$ mice were used as control mice. All cells in these mTmG reporter mice exhibit a cell membrane-localized tdTomatoRed (mT) fluorescence signal before Cre recombination. Following Cre

recombinase activity, myeloid cells (and their future lineages) show cell membrane-localized EGFP (mG) fluorescence, replacing the initial red fluorescence signal.

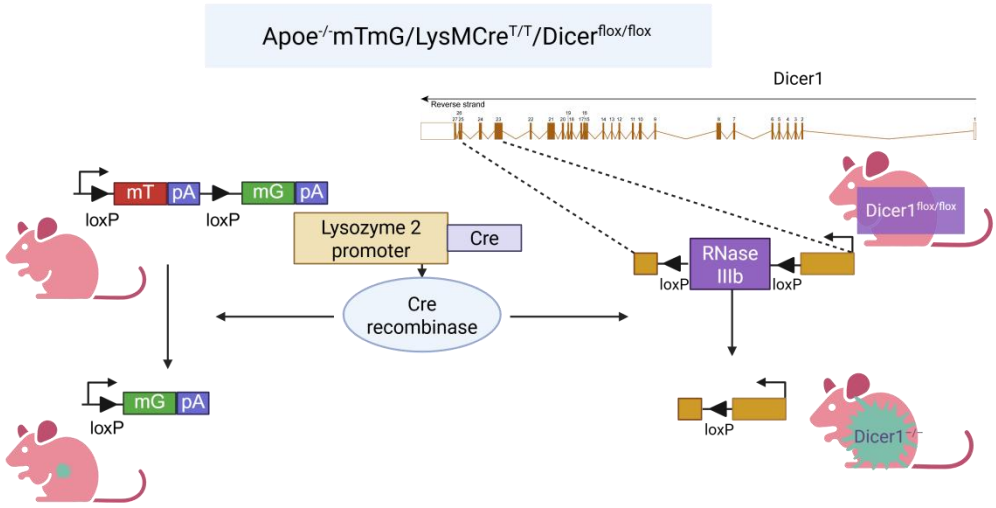

Fig. 5: Generation of Apoe$^{-/-}$mTmG/LysMCre$^{T/T}$/Dicer$^{flox/flox}$ mice

Apoe$^{-/-}$/LysMCre$^{T/T}$/Dicer$^{flox/flox}$ mice were generated by crossing Apoe$^{-/-}$ mice expressing Cre recombinase under the control of the myeloid-specific lysozyme M promoter with Dicer$^{flox/flox}$ mice. To visualize Cre activity, mice were further crossed with mTmG reporter mice, where membrane-targeted tdTomatoRed (mT) is expressed in all cells before recombination. Upon Cre activation, tdTomatoRed is excised and replaced with membrane-targeted EGFP (mG) specifically in myeloid cells. This strategy allows genetic deletion of Dicer in macrophages and simultaneous fluorescent tracking of Cre-expressing cells.

Moreover, Apoe$^{-/-}$/LysMCre$^{T/T}$/Dicer$^{flox/flox}$ mice were crossed with mice carrying a GFP-tagged Argonaute 2 transgene under the control of a loxP-flanked stop cassette (LSL-tAgo2, Strain #:017626, The Jackson Laboratory)[70] to obtain Apoe$^{-/-}$/tAgo2$^{T/T}$/LysMCre$^{T/T}$/Dicer$^{flox/flox}$ mice (Fig. 6), in which tAGO2 is specifically expressed in myeloid cells upon Cre-mediated recombination. Apoe$^{-/-}$/tAgo2$^{T/T}$/LysMCre$^{T/T}$/Dicer$^{WT/WT}$ mice were used as control mice. Male and female mice aged 6-8 weeks were fed a western-type diet (WD) comprising 21% fat, 19.5% casein, and 0.15% cholesterol (Ssniff Spezialdiäten GmbH) for 12 or 24 weeks. All mice were maintained under controlled conditions with a 12-hour light phase (7:00 a.m. to 7:00 p.m.) and a 12-hour dark phase (7:00 p.m. to 7:00 a.m.), and were provided with ad libitum access to food and water. All animal procedures were conducted in accordance with German animal welfare regulations and were

approved by the local authorities (approval numbers ROB-55.2Vet-2532. Vet_02-20-67 District Government of Upper Bavaria).

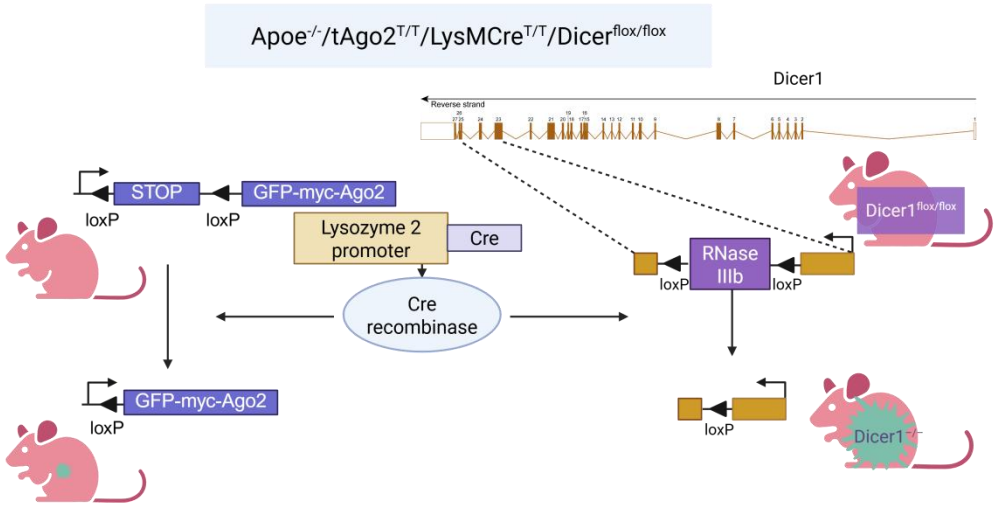

Fig. 6: Generation of Apoe$^{-/-}$/tAgo2$^{T/T}$/LysMCre$^{T/T}$/Dicer$^{flox/flox}$ mice

Apoe$^{-/-}$/LysMCre$^{T/T}$/Dicer$^{flox/flox}$ mice were crossed with Rosa26^{tAGO2} knock-in mice to study Dicer-mediated regulation of miRNA targets in macrophages. Cre recombination in myeloid cells induces both the deletion of Dicer and the expression of GFP-myc-tagged Ago2. This allows for myeloid cell-specific tAgo2 immunoprecipitation in macrophages in vivo. Schematic illustration created with BioRender.com.

2.4 4D live plaque imaging and analysis

2.4.1 4D live plaque imaging

Aortic arch or root tissues containing plaques were harvested from Apoe$^{-/-}$mTmG/LysMCre$^{T/T}$/Dicer$^{flox/flox}$ and Apoe$^{-/-}$mTmG/LysMCre$^{T/T}$/Dicer$^{WT/WT}$ mice following 12 or 24 weeks of WD feeding (Fig. 7). The live tissues were immediately placed into a chamber slide (µ-Slide 4 Well Glass Bottom, Ibidi) containing medium (DMEM supplemented with 10% FBS and 5% L929 supernatant) with the luminal side downwards (Fig. 7). Live plaque imaging was conducted using confocal laser scanning microscopy (Leica SP8 3X, Leica Microsystems) with a white light laser, a 63x/1.40 plan-apo oil objective, and hybrid diode detectors (Fig. 7). Throughout imaging, tissues were kept at 37°C in a climate chamber with 5% CO_2. All fluorescent targets were recorded in individual spectral channels and acquired in sequential mode with

optimized excitation and emission parameters: BioTracker NucView® 405 Caspase-3 and BioTracker 405 Blue Mitochondria dye (excitation: 405nm, detection: 410-478nm); LipidSpot™ 610, MitoView™ 633 dye, MitoTracker™ Deep Red FM (excitation: 612nm, detection: 617-729nm); EGFP (excitation: 488nm, detection: 493-557nm); TomatoRed and Human DiI high oxidized LDL (excitation: 554nm, detection: 559-616nm). Crystals were detected using confocal reflection microscopy, with the reflection light captured by placing the detector channel over the wavelength of the selected laser channel (excitation: 488nm, detection: 486-491nm). Spectral channel settings were chosen to optimize intensity while limiting bleed-through and background noise. Images with a z-stack up to 30 µm and a time up to seven hours were acquired to represent plaque overview and activity in real time in reconstructed 3D z-projections. The raw images were deconvolved using the lightning algorithms of the acquisition software Leica Application Suite X (LAS X 3.4; Leica Microsystems). Image processing was performed with LAS X 3.7 (Leica Microsystems) to generate the final representative images and videos.

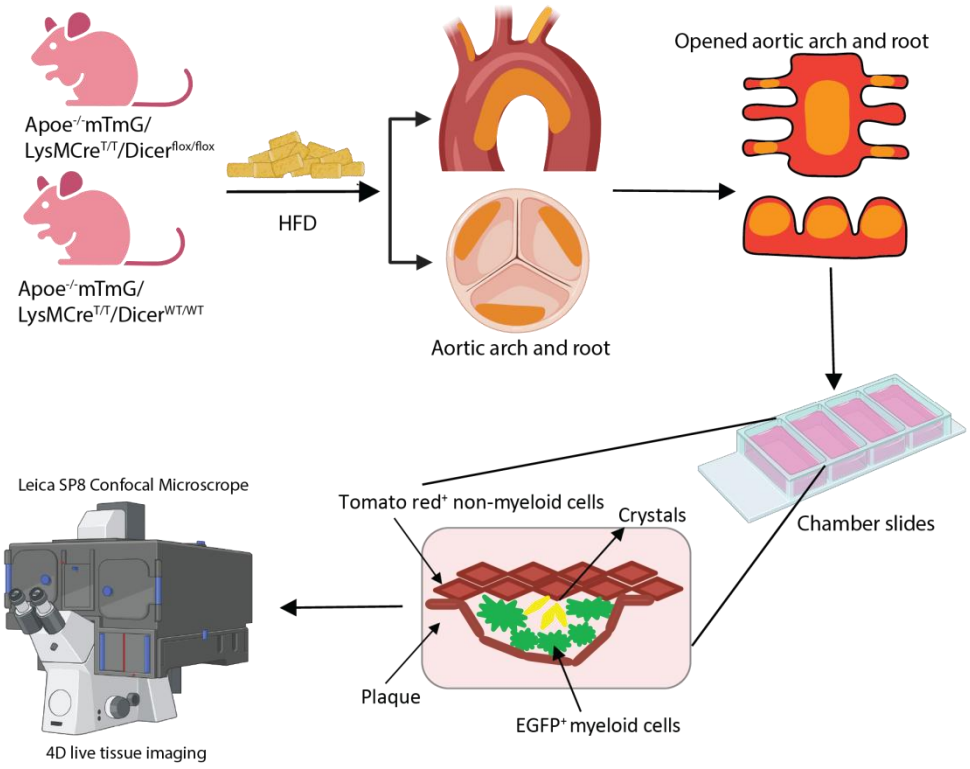

Fig. 7: Schematic overview for live imaging of atherosclerotic plaques

Aortic arch and root tissues were harvested from WD-fed Apoe$^{-/-}$mTmG/LysMCre$^{T/T}$/Dicer$^{flox/flox}$ and Apoe$^{-/-}$mTmG/LysMCre$^{T/T}$/Dicer$^{WT/WT}$ mice mice, cut open to expose the luminal surface with plaques, and mounted luminal side down in chamber slides. Live plaques were imaged using confocal laser

scanning microscopy under physiological conditions maintained at 37 °C with controlled CO_2 supply, allowing visualization of EGFP$^+$ myeloid cells, TomatoRed$^+$ non-myeloid cells, and CCs. Schematic illustration created with BioRender.com.

2.4.2 Lipid droplet analysis

LipidSpot^{TM} 610 (Biotium) was used to stain lipid droplets. The Lipidspot-positive area in EGFP-positive cells (central 2-3 z-stacks without nuclei area) was quantified in confocal images of mouse plaques using Fiji (ImageJ, version 2.3.0). The individual LD size in the plaque macrophages was determined in 3D reconstructions of the confocal images using the LASX 3D Analysis module (Leica).

2.4.3 Mitochondria analysis

Dyes that label mitochondria with an intact mitochondrial membrane potential (BioTracker 405 Blue Mitochondria dye, Sigma-Aldrich, and MitoViewTM 633, Biotium) were used to visualize mitochondrial activity. MitoTracker^{TM} Deep Red FM (Thermo Fisher Scientific) was used to label mitochondrial morphology. BioTracker 405 signal-positive area in EGFP-positive cells (central 2-3 z-stacks without nuclei area) was quantified in confocal images of mouse plaques using Fiji (ImageJ, version 2.3.0).

2.4.4 oxLDL uptake analysis

Dil-labeled oxidized LDL (Dil-oxLDL; Kalen Biomedical) was added to plaque tissue during live imaging to assess the oxLDL uptake capacity of plaque macrophages. Co-localization of the red Dil-oxLDL signal with green EGFP signal was identified as oxLDL uptake by macrophages and quantified using 3D image analysis in the Leica Application Suite X software (version 3.7.5).

2.4.5 Apoptosis analysis

The dye consists of a fluorogenic DNA dye coupled to the caspase-3/7 DEVD recognition sequence, which will stain DNA after being cleaved by caspase-3/7 (BioTracker NucView® 405 Caspase-3, Sigma-Aldrich). This was used to indicate caspase 3 and 7 activity and visualize DNA morphology and distribution after caspase 3 and 7 activation. Caspase3-positive plaque macrophages (EGFP positive) were

counted in the plaque region using Fiji (ImageJ, version 2.3.0). Extracellular DNA stained with the caspase-3 dye was quantified as caspase-3 dye-positive regions that did not overlap with TomatoRed or EGFP signals, using 3D image analysis in LASX.

2.5 Seahorse assay

To assess mitochondrial function of the aorta tissue, the oxygen consumption rate (OCR) was measured using the Seahorse XFe24 Analyzer. One day before measurement, the sensor cartridge was hydrated with Seahorse XF Calibrant in a non-CO2 incubator at 37 °C overnight. Plaques from the lower curvature of the aortic arch, and the adjacent normal aortic tissue were harvested from $Apoe^{-/-}/LysMCre^{T/T}/Dicer^{flox/flox}$ and $Apoe^{-/-}/LysMCre^{T/T}/Dicer^{WT/WT}$ mice following 24 weeks of WD feeding. Subsequently, each plaque tissue was immediately put into one well of the Seahorse XFe24 Islet Capture FluxPak containing 500 µL assay medium (supplemented with Seahorse XF DMEM, 1M Seahorse XF Glucose, 100 mM Seahorse XF Pyruvate, and 200 mM Seahorse XF L-Glutamine). Tissues were stabilized in the well by capture screens. Next, the plate containing tissues was placed in the non-CO2 incubator at 37 °C for 60 minutes before measurement. The following drugs were injected through ports in the Seahorse Flux Pak cartridges during measurement: Oligomycin (4 µM), carbonyl cyanide 4-(trifluoromethoxy) phenylhydrazone (FCCP; 1 µM), rotenone (5 µM), and antimycin A (5 µM). After measurement, the tissue was fixed in 4% PFA and imaged using inverted Thunder microscopy (Leica). Tissue size was quantified by Image J. OCRs were normalized to tissue size. Basal and maximal respiration, spare respiratory capacity (SRC), ATP production, non-mitochondrial respiration, and proton leak were analyzed using Agilent XF Seahorse Analytics (https://seahorseanalytics.agilent.com/).

2.6 Lipid and CC analysis in murine aorta

Following overnight fixation and removal of the adventitia, the aorta was opened along its longitudinal axis, and the en-face was stained with Oil Red O to visualize lipid accumulation. Imaging of the whole aorta was subsequently performed using a Leica DM6 B Thunder upright microscope (Leica). Bright-field images for lipid visualization were acquired with a DFC365 FX camera, while CC was visualized under polarized light using a K5 camera in combination with a polarizing filter.

Crystal-positive areas within Oil Red O-stained regions were quantified using Fiji (ImageJ, version 2.3.0).

2.7 Cell culture

Bone marrow cells were isolated from the femurs and tibias of $Apoe^{-/-}/LysMCre^{T/T}/Dicer^{flox/flox}$ or $Apoe^{-/-}/LysMCre^{T/T}/Dicer^{WT/WT}$ mice. The cells were then cultured in DMEM/F12 medium supplemented with 10% FBS and 10% L929-conditioned medium for 7 days to induce the differentiation into BMDMs.

To generate oxidized low-density lipoproteins (oxLDL), human low-density lipoproteins (LDL; Merck) were dialyzed using D-tube Midi Dialyzer tubes (Merck) for 24 hours at 4 °C to remove EDTA. After dialysis, LDL was oxidized by incubation with 10 µM $CuSO_4$ at 37 °C. The absorbance at 234 nm was measured using a Spectrophotometer (Implen). The oxidation reaction was terminated by adding 20 µM EDTA when the absorbance at 234 nm did not change in three consecutive measurements within one and a half hours. The resulting oxLDL was then purified using a PD-10 desalting column (Cytiva) to remove residual EDTA and $CuSO_4$, and stored at 4 °C for up to one week until use. Foam cell was induced by incubating the BMDMs with oxLDL (100 µg/ml) for 72 hours. Inflammatory macrophages were induced by stimulating BMDMs with LPS (100 ng/ml, Merck) for 22 hours and 10 ng/ml IFN-γ (PeproTech) for 16 hours.

2.8 Liquid chromatography-tandem mass spectrometry (LC-MS/MS)

LPS/IFN-γ-treated and oxLDL-treated BMDMs from $Apoe^{-/-}/LysMCre^{T/T}/Dicer^{flox/flox}$ and $Apoe^{-/-}/LysMCre^{T/T}/Dicer^{WT/WT}$ mice were harvested, pelleted, and frozen until further use. The cell pellets were subsequently transferred to the ZfP facility of the LMU Biomedical Center to conduct LC-MS/MS analysis, following the protocol described by Kaseder et al[71]. The detected proteins from $Apoe^{-/-}/LysMCre^{T/T}/Dicer^{flox/flox}$ mice and $Apoe^{-/-}/LysMCre^{T/T}/Dicer^{WT/WT}$ mice groups were compared using the Limma package within ImShot (version 1.0.1). Proteins showing a fold change (FC) greater than 1.3 and an adjusted P-value less than 0.05 were considered significantly different between the groups. Pathway enrichment analysis for differentially expressed proteins was conducted using Ingenuity Pathway Analysis (IPA, Qiagen) or g: Profiler (https://biit.cs.ut.ee/gprofiler_archive3/e98_eg45_p14/gost) to identify significantly

enriched pathways and biological processes. Pathway activation states were predicted using the IPA z-score algorithm, with thresholds of z-score > 2 or < −2 indicating predicted activation or inhibition, respectively.

2.9 GFP-tagged Ago2-IP-seq

To identify the targets of Dicer-generated miRNAs, I conducted GFP-tagged Ago2 immunoprecipitation (IP) of arteries and BMDMs using Apoe$^{-/-}$/tAgo2$^{T/T}$/LysMCre$^{T/T}$/Dicer$^{flox/flox}$ and Apoe$^{-/-}$/tAgo2$^{T/T}$/LysMCre$^{T/T}$/Dicer$^{WT/WT}$ mice. The target mRNAs of Dicer-mediated miRNAs in plaque macrophages or BMDMs were enriched in the IP samples. To prepare artery samples, carotids, aortas, and aortic roots from each mouse were harvested and pooled. The tissues were minced into small fragments and transferred into pre-chilled safe-lock tubes containing lysis buffer, protease inhibitor, and RNaseout. The tubes were then placed in the pre-chilled tissue lyzer (Qiagen) and homogenized at 50 Hz for two minutes, followed by one minute at 50 Hz, to ensure thorough disruption. Following homogenization, samples were incubated on ice for 15 minutes and centrifuged at 7,000 x g for 15 minutes at 4 ° C. To prepare BMDM samples, BMDMs were harvested and incubated with lysis buffer containing protease inhibitor and RNaseout for 20 min at 4°C and centrifuged at 7,000 x g for 15 minutes at 4 °C. After centrifugation, the supernatant from aorta and BMDMs samples were collected, with an aliquot from each stored as before IP (BIP) control, and the remaining lysates were used for subsequent immunoprecipitation. Following sample preparation, tAGO2 was immunoprecipitated using GFP-Trap agarose beads (Chromotek, Proteintech) containing agarose beads coupled with a GFP Nanobody/VHH. Briefly, sample lysates were incubated with GFP-Trap agarose beads for two hours at 4 ° C on a rocking platform, and subsequently washed thoroughly to remove non-specific bindings. Bound complexes were eluted using acidic elution buffer, immediately neutralized with Tris buffer (1 M, pH 10.4), and centrifuged to collect the supernatant as the after IP (AIP) samples. According to the manufacturer's protocol, RNA was then extracted from the BIP and AIP samples using the PicoPure RNA Isolation Kit (Thermo Fisher Scientific). The concentration and purity of isolated RNA were measured with a spectrophotometer (Implen), and samples were stored at -80 °C until use. After collection, all IP samples were submitted to the Anthropology and Human Genomics department of LMU for Prime-sequencing, as previously developed and described by Janjic et al[72]. For analysis, the RNA read count ratio of AIP to BIP was calculated to represent RNA RISC abundance in BMDM IP samples,

and the AIP read counts were used to indicate RNA RISC abundance in aorta tissue IP samples.

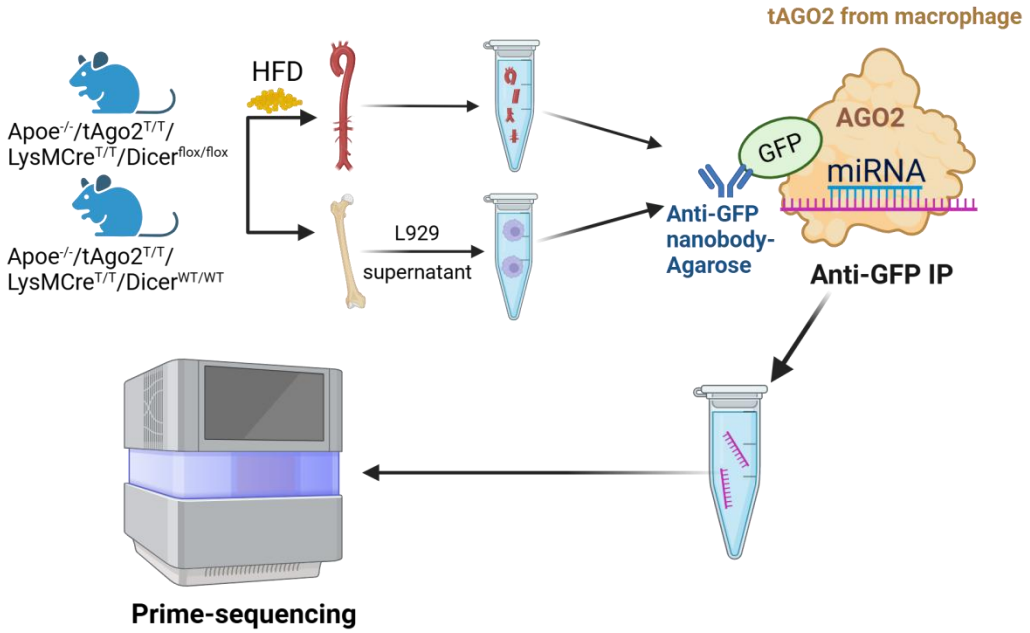

Fig. 8: Workflow of GFP-tagged Ago2-IP-seq

Aortic tissues (including carotid, aorta, and root) and BMDMs were isolated from Apoe$^{-/-}$/tAgo2$^{T/T}$/LysMCre$^{T/T}$/Dicer$^{flox/flox}$ and Apoe$^{-/-}$/tAgo2$^{T/T}$/LysMCre$^{T/T}$/Dicer$^{WT/WT}$ mice. After tissue lysis and homogenization, GFP-tagged AGO2 complexes were immunoprecipitated using GFP nanobody-conjugated agarose (GFP-Trap). Co-immunoprecipitated RNA within the RISC was purified and used for RNA sequencing to identify mRNAs targeted by Dicer-mediated miRNAs in myeloid cells. Schematic illustration created with BioRender.com.

2.10 Automated Western Blot (JESS)

To assess target protein expression in tissues or cells, I conducted the automated capillary-based western blotting system (JESS, ProteinSimple, USA) according to the manufacturer's protocol. Briefly, cell or tissue lysates were prepared using lysis buffer, and protein concentrations were determined using the DC protein assay (Bio-Rad Laboratories). Prior to analysis, protein samples were mixed with fluorescent master mix and DTT and denatured by heating at 95 ° C for 5 minutes.

Subsequently, protein samples and biotinylated ladder were loaded onto the pre-filled plate (12-230 kDa Separation Module, ProteinSimple). GFP antibodies (Rockland), pSTAT1 antibodies (Invitrogen), secondary antibodies (anti-rabbit HRP conjugate, ProteinSimple; anti-mouse HRP conjugate, ProteinSimple; streptavidin-HRP conjugate, Bio-techne) were loaded into the plate. The mixture of luminol-S and peroxide (Thermofisher Scientific) was loaded for chemiluminescent detection. Protein normalization reagents (ProteinSimple) were loaded onto the plate as internal controls for protein loading normalization. After all the loading, the plate was installed in the Jess system (ProteinSimple's Jess, Bio-techne) for automatic protein separation, immobilization, immunoprobing, and chemiluminescence detection. Target protein signals were quantified based on the area under the curve (AUC) of the chemiluminescent peaks and normalized to the total protein signal from the normalization reagent using *Compass for Simple Western software* (ProteinSimple).

2.11 Mitochondrial DNA detection

To assess cytosolic release of mitochondrial DNA (mtDNA) in LD-containing macrophages, the cytosolic level of a representative mtDNA, cytosolic cytochrome c oxidase I was quantified by quantitative PCR (qPCR). Briefly, oxLDL-treated BMDMs from $Apoe^{-/-}$/$LysMCre^{T/T}$/$Dicer^{flox/flox}$ and $Apoe^{-/-}$/$LysMCre^{T/T}$/$Dicer^{WT/WT}$ mice were harvested and resuspended in PBS. One-tenth of the cell suspension was used for total DNA extraction, while the remaining cell suspension was processed for cytosolic DNA isolation.

To prepare the cytosolic fraction, I used the Mitochondria Isolation Kit for Cultured Cells (Thermo Scientific). The cell suspension was centrifuged at 300 g to remove supernatant, and the cell pellet was resuspended in Reagent A, followed by brief vortexing and incubation on ice to initiate plasma membrane disruption. Reagent B was then added to halt the lysis reaction and preserve mitochondrial integrity, followed by Reagent C to facilitate mitochondrial stabilization before differential centrifugation. The homogenate was first centrifuged at 700 g for 10 minutes to remove nuclei and intact cells, and then at 12,000 g for 15 minutes to pellet mitochondria. The resulting supernatant was collected as the cytosolic fraction. For preparation of the total fraction, the cell suspension was centrifuged at 300 g to remove supernatant and resuspended in PBS containing proteinase K to degrade proteins.

DNA was extracted using the DNeasy Blood & Tissue Kit (Qiagen). The total fraction was incubated with Buffer AL at 56 °C for 10 min. Ethanol (96-100%) was then added to the total and cytosolic fractions, and the mixtures were vortexed thoroughly to obtain homogeneous solutions. DNA was purified using column-based extraction per the manufacturer's instructions, eluted in nuclease-free water, and quantified using a NanoPhotometer (Implen).

qPCR was performed to detect the mtDNA-encoded gene cytochrome c oxidase I, using specific primers (forward: 5'- GCCCCAGATATAGCATTCCC -3'; reverse: 5'-GTTCATCCTGTTCCTGCTCC -3'). Amplification was conducted using GoTaq® qPCR and RT-qPCR Systems (Promega) on a QuantStudio™ 6 Flex Real-Time PCR System (Qiagen). To account for potential contamination and variation in DNA input, mtDNA levels detected in the cytosolic fraction were normalized to the total DNA content (from the total cell fraction) of each corresponding sample. Relative cytosolic mtDNA levels were then compared between $Apoe^{-/-}$/$LysMCre^{T/T}$/$Dicer^{flox/flox}$ and $Apoe^{-/-}$/$LysMCre^{T/T}$/$Dicer^{WT/WT}$ mice groups using the ΔΔCt method.

2.12 Immunostaining

Sections of paraformaldehyde-fixed, paraffin-embedded murine aortic root sections were deparaffinized in xylene and rehydrated through a graded ethanol series to distilled water. For antigen retrieval, the sections were heated in citrate buffer (pH 6) in the microwave at 600W for 20 min, then gradually cooled to room temperature. After rinsing with PBS, sections were blocked with 1% bovine serum albumin in PBS for 30 minutes at room temperature to avoid non-specific antibody binding. Sections were then incubated with anti-Ftl1 antibody (Proteintech) and anti-Mac2 antibody (in-house preparation, supernatant from hybridoma cell line M3/38.1.2.8 HL.2) overnight at 4° C in a humidified chamber. The following day, sections were washed thoroughly with PBS and then incubated with secondary antibodies conjugated with a fluorescent dye, such as anti-rat-FITC (Jackson ImmunoResearch) and anti-Rabbit-Cy3 (Jackson ImmunoResearch), for 30 min at room temperature in the dark. Sections were subsequently washed with PBS and mounted using Vectashield mounting medium containing DAPI (Vector Laboratories). Fluorescent images were acquired using a confocal laser scanning microscope.

2.13 Binding site analysis/prediction

To identify possible miRNA binding sites for the target mRNAs, their 3' untranslated region (3'-UTR) sequences were retrieved from the Ensembl database (*https://www.ensembl.org/index.html*). The sequence of all murine miRNAs was taken from miRBase 22.1 (*http://www.mirbase.org/*). Subsequently, miRNA target site prediction was performed using RNAhybrid (*https://bibiserv.cebitec.uni-bielefeld.de/rnahybrid*), including the identification of both canonical sites (8-mer, 7-mer-m8, and 7-mer-A1, defined by perfect seed pairing without G: U wobble and a helical constraint from nucleotides 2-7) and non-canonical sites (based on the helical constraint from nucleotides 2-7). In addition, TargetScanMouse version 8.0 (*http://www.targetscan.org/vert_80/*) was used to predict evolutionarily conserved miRNA binding sites based on seed sequence complementarity and cross-species conservation.

2.14 Statistical analysis

Statistical analysis was performed using Prism 10 software (GraphPad Software, USA). Prior to analysis, the Shapiro-Wilk test (n<5) and the Kolmogorov-Smirnov test (n>5) were used to test whether the data are normally distributed. All data are shown as mean ± standard deviation (SD). For comparisons between two independent groups, Student's t-tests were performed. Comparisons for more than two groups were performed using one-way ANOVA, followed by Fisher's LSD test. Comparisons of proteomics data were performed using Limma (ImShot_1.0.1), including analyses between $Apoe^{-/-}$/$LysMCre^{T/T}$/$Dicer^{flox/flox}$ mice and $Apoe^{-/-}$/$LysMCre^{T/T}$/$Dicer^{WT/WT}$ mice groups, and between LPS/IFN-γ-treated and oxLDL-treated BMDMs within the $Apoe^{-/-}$/$LysMCre^{T/T}$/$Dicer^{WT/WT}$ mice. RNA RISC abundance was compared between $Apoe^{-/-}$/$tAgo2^{T/T}$/$LysMCre^{T/T}$/$Dicer^{flox/flox}$ and $Apoe^{-/-}$/$tAgo2^{T/T}$/$LysMCre^{T/T}$/$Dicer^{WT/WT}$ mice groups in BMDMs using multiple t-tests with a 1% FDR, controlled by the two-stage linear step-up procedure of Benjamini, Krieger, and Yekutieli, and in aortas using one-tailed multiple t-tests. Differentially expressed miRNAs in oxLDL-treated BMDMs between $Apoe^{-/-}$/$LysMCre^{T/T}$/$Dicer^{flox/flox}$ and $Apoe^{-/-}$/$LysMCre^{T/T}$/$Dicer^{WT/WT}$ mice groups were compared using multiple t-tests with Holm-Šídák correction. For IPA analysis, statistical significance was determined using Fisher's exact test with Benjamini-Hochberg multiple comparison correction to control the FDR. For *g: Profiler* analysis, the significance of enrichment was determined using the g: SCS multiple testing correction method, with an adjusted P-value (FDR) threshold of < 0.05. The analysis was performed using the default background set provided by g: Profiler.

3. Result

3.1 Effect of Dicer on lipid accumulation in plaque macrophages

The previous study indicates that Dicer reduces lipid accumulation in plaque macrophages, probably due to the regulation of mitochondrial activity[65]. However, the exact mechanism of this Dicer effect is unclear. In this study, 4D live plaque imaging was performed utilizing mTmG reporter Apoe$^{-/-}$ mice to investigate the impact of Dicer knockout on mitochondrial activity and lipid droplet accumulation. Based on the lipid droplet (LD) content, plaque macrophages were classified into three subgroups: 30% contained less than 5% LDs (LD^{low}), 20% contained 5-20% LDs (LD^{inter}), and around 50% contained more than 20% LDs (LD^{high}, Fig. 9A and B). Moreover, the area of active mitochondria was reduced in LD^{high} and LD^{inter} macrophages compared to LD^{low} macrophages (Fig. 9A and C).

To confirm the mitochondrial activity analysis from the live plaque imaging, OCR of the aortic arch tissue with or without plaque was measured using a Seahorse assay. In the presence of plaques, spare respiration capacity was lower, while the proton leak was higher than in normal aortic arches (Fig. 9D). This result suggests a lower level of mitochondrial respiration and a higher level of mitochondrial uncoupling in LD^{high} macrophages, the most abundant plaque cell type. Taken together, these findings indicate that LD accumulation impairs mitochondrial function in macrophages.

Next, I explored whether Dicer regulates the LD accumulation in plaque macrophages. To this end, I conducted live plaque imaging utilizing mTmG reporter Apoe$^{-/-}$ mice with a myeloid cell-specific Dicer knockout. Dicer knockout increased the LDhigh and reduced the LDlow macrophage fraction (Fig. 9E), suggesting that Dicer limits the formation of LD-containing macrophages.

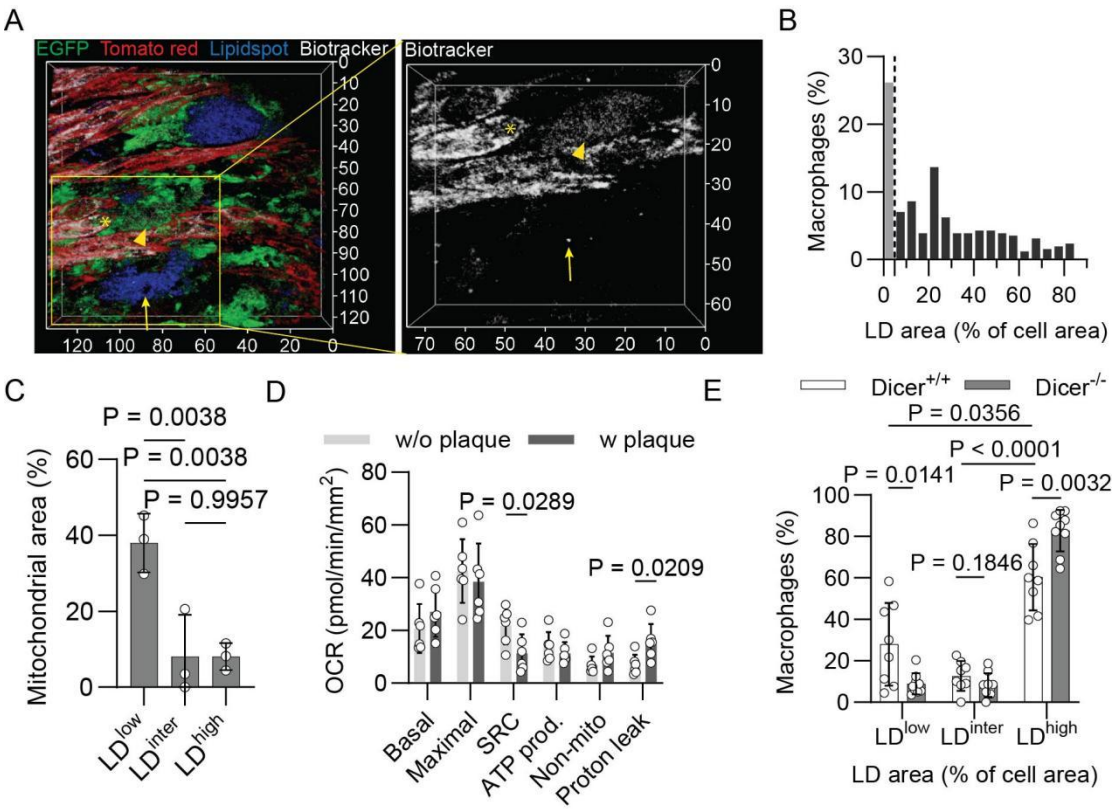

Fig. 9: Dicer knockout increased lipid accumulation in plaque macrophages

(A) 3D view of an arch plaque from an Apoe$^{-/-}$mTmG/LysMCre$^{T/T}$/Dicer$^{WT/WT}$ mouse, with LDs stained by lipidspot and mitochondria by BioTracker 405 Blue Mitochondria (Biotracker). Arrow, an LD-containing macrophage with low mitochondrial activity; arrowhead, a non-LD-containing macrophage with high mitochondrial activity; asterisk, an EC with high mitochondrial activity. (B) LD content in plaque macrophages was analyzed. The percentage of LD area within the macrophage area was determined in 256 plaque macrophages from 9 mice. (C) Active mitochondria content of plaque macrophages, determined by the BioTracker 405 Blue Mitochondria dye, shown as mitochondria-positive area in the macrophage. Statistical significance was determined by one-way ANOVA with Fisher's LSD test (n=3 mice per group). (D) OCR in aortic arch tissues with or without plaques from Apoe$^{-/-}$/LysMCre$^{T/T}$/Dicer$^{WT/WT}$ mice was measured by Seahorse assay. Basal and maximal respiration, SRC, ATP production, non-mitochondrial respiration, and proton leak were compared between the two groups using Student's t-test (n=6 mice per group). (E) Macrophage subtype ratios were compared between plaques from Apoe$^{-/-}$mTmG/LysMCre$^{T/T}$/Dicer$^{flox/flox}$ (Dicer$^{-/-}$) and Apoe$^{-/-}$mTmG/LysMCre$^{T/T}$/Dicer$^{WT/WT}$ (Dicer$^{+/+}$) mice using Student's t-test, three subtypes in each genotype were compared by one-way ANOVA with Fisher's LSD test (n=8-9 mice per group).

3.2 Effect of Dicer on LD size and oxLDL uptake

Next, I investigated whether Dicer affects LD^{high} macrophage accumulation by regulating LD size. Dicer knockout increased LD size by more than twofold in

macrophages (Fig. 10A), suggesting Dicer inhibits LD expansion, which contributes to limiting the formation of LD^{high} macrophages. Moreover, most of the LDs contained crystals in their core region, probably CCs (Fig. 10 B), indicating that crystal formation contributes to the effect of Dicer knockout on LD growth.

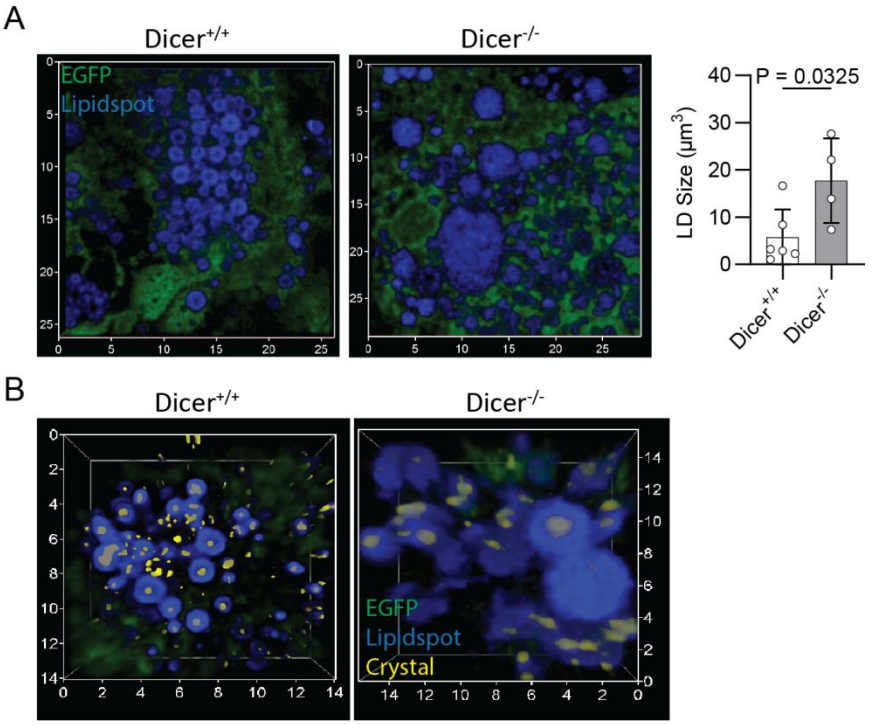

Fig. 10: Dicer knockout increased LD size in plaque macrophages

Live plaque imaging was performed for aortic arch tissue with plaques from $Apoe^{-/-}$mTmG/LysMCre$^{T/T}$/Dicer$^{flox/flox}$ ($Dicer^{-/-}$) and $Apoe^{-/-}$mTmG/LysMCre$^{T/T}$/Dicer$^{WT/WT}$ ($Dicer^{+/+}$) mice. 3D reconstructions of the z-stacks are shown. (A) Volume of individual LDs in macrophages was determined after staining with Lipidspot. Statistical significance was determined by Student's t-test (n=4-6 mice per group). (B) Crystals were detected by reflection confocal microscopy in macrophage LDs.

To investigate whether oxLDL uptake contributes to LD formation, plaque tissue was incubated with DiI-labeled oxLDL before live imaging. oxLDL co-localized with LDs, indicating that oxLDL uptake facilitates LD formation. Then I checked whether Dicer reduced LD size by affecting oxLDL uptake. Notably, the amount of oxLDL in plaque macrophages did not differ between $Apoe^{-/-}$mTmG/LysMCre$^{T/T}$/Dicer$^{flox/flox}$ and $Apoe^{-/-}$mTmG/LysMCre$^{T/T}$/Dicer$^{WT/WT}$ mice (Fig. 11), indicating that Dicer does not limit LD accumulation in macrophages by regulating oxLDL uptake.

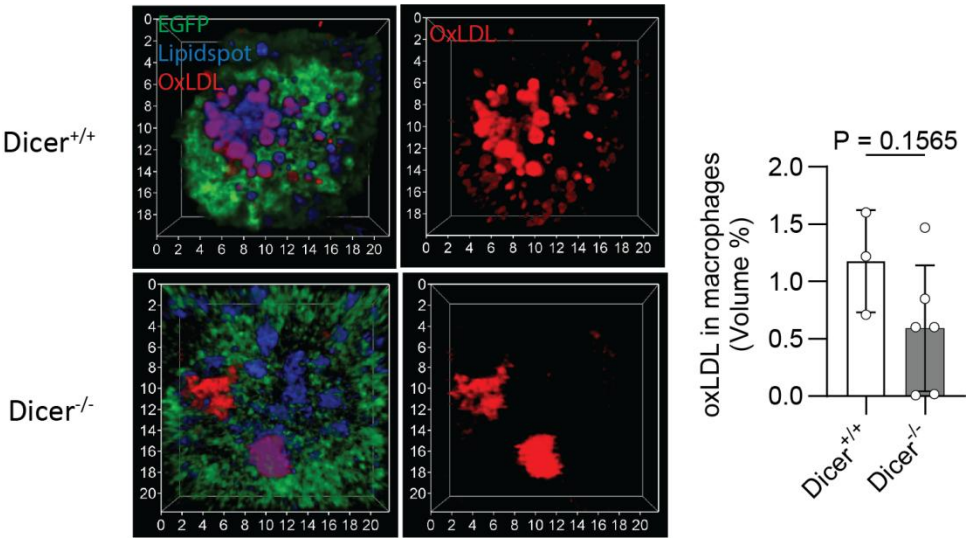

Fig. 11: Dicer knockout did not affect the uptake of oxLDL by plaque macrophages.

Live plaque imaging was conducted on aortic arch tissues with plaques from Apoe$^{-/-}$mTmG/LysMCre$^{T/T}$/Dicer$^{flox/flox}$ (Dicer$^{-/-}$) and Apoe$^{-/-}$mTmG/LysMCre$^{T/T}$/Dicer$^{WT/WT}$ (Dicer$^{+/+}$) mice after incubation with Dil-labeled oxLDL. A representative 3D reconstruction of the z-stacks is displayed. The volume of Dil-labeled oxLDL in macrophages was compared between Apoe$^{-/-}$mTmG/LysMCre$^{T/T}$/Dicer$^{flox/flox}$ (Dicer$^{-/-}$) and Apoe$^{-/-}$mTmG/LysMCre$^{T/T}$/Dicer$^{WT/WT}$ (Dicer$^{+/+}$) mice using Student's t-test (n=3-6 mice per group).

3.3 Role of Dicer in mitochondrial function in macrophages

To investigate how Dicer influences the mitochondrial function of plaque macrophages, I incorporated mitochondrial membrane potential dyes together with LipidSpot during live plaque imaging. Notably, Dicer knockout reduced mitochondrial activity in both LD^{high} and LD^{low} plaque macrophages (Fig. 12A, B). Consistent with this finding, measurement of the OCR in plaques by Seahorse assay showed that Dicer knockout reduced basal respiration, maximal respiration, and ATP production (Fig. 12C), suggesting that Dicer promotes mitochondrial respiration in different macrophage subtypes.

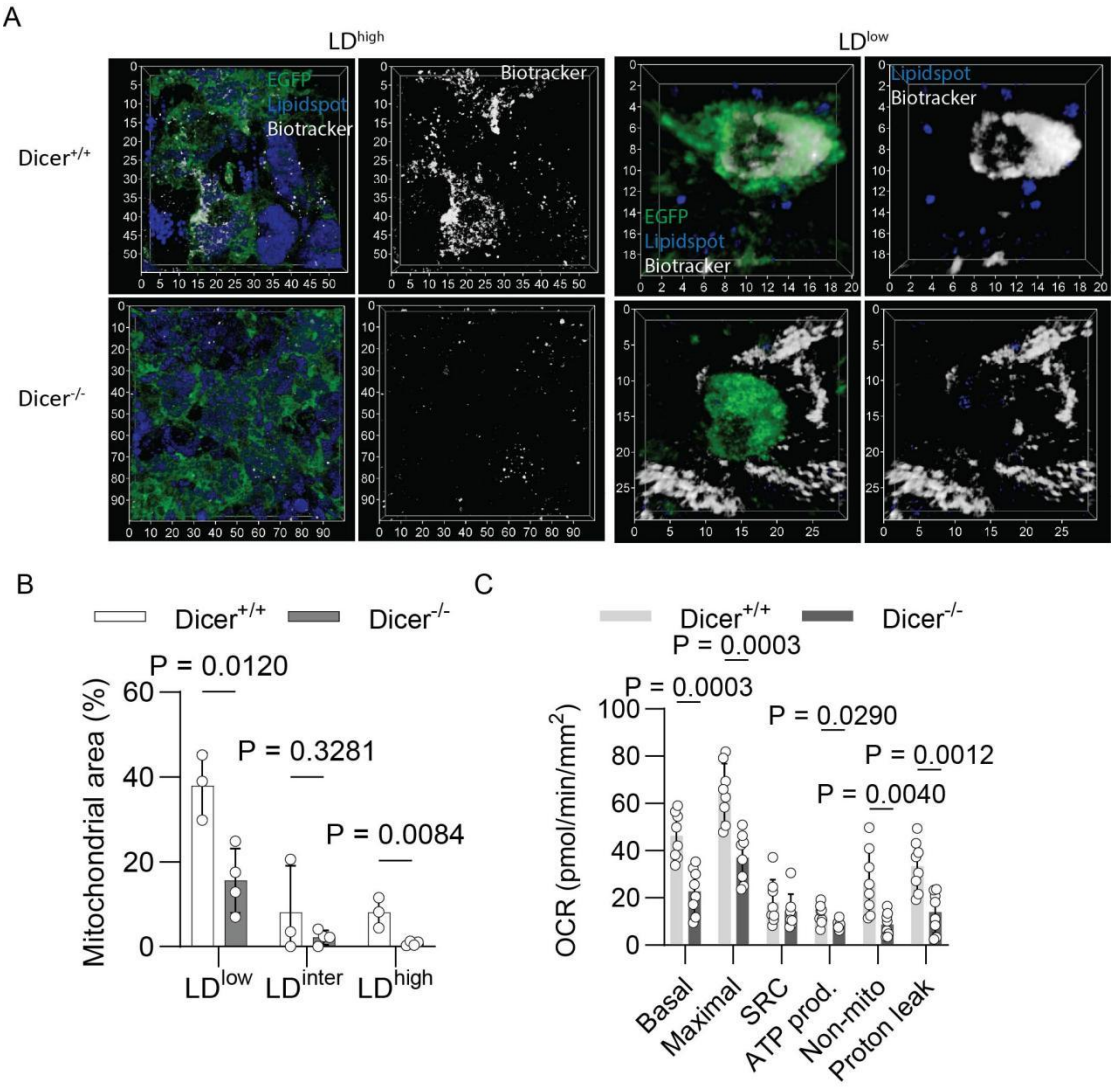

Fig. 12: Dicer knockout decreased the mitochondrial activity of plaque macrophages.

(A) Live plaque imaging was performed on aortic arch tissues with plaques from Apoe$^{-/-}$mTmG/LysMCre$^{T/T}$/Dicer$^{flox/flox}$ (Dicer$^{-/-}$) and Apoe$^{-/-}$mTmG/LysMCre$^{T/T}$/Dicer$^{WT/WT}$ (Dicer$^{+/+}$) mice, with LDs stained by lipidspot and mitochondria by BioTracker 405 Blue Mitochondria (Biotracker). A 3D reconstruction of the z-stacks is shown. (B) The mitochondrial activity of plaque macrophage subtypes was assessed using Biotracker 405 Blue Mitochondria dye and compared between Apoe$^{-/-}$mTmG/LysMCre$^{T/T}$/Dicer$^{flox/flox}$ (Dicer$^{-/-}$) and Apoe$^{-/-}$mTmG/LysMCre$^{T/T}$/Dicer$^{WT/WT}$ (Dicer$^{+/+}$) mice using a Student's t-test (n = 3-4 mice per group). (C) The oxygen consumption rate (OCR) in aortic arch tissues with plaques from Apoe$^{-/-}$/LysMCre$^{T/T}$/Dicer$^{flox/flox}$ (Dicer$^{-/-}$) and Apoe$^{-/-}$/LysMCre$^{T/T}$/Dicer$^{WT/WT}$ (Dicer$^{+/+}$) mice was assessed using Seahorse assay. Basal and maximal respiration, SRC, ATP production (ATP prod.), non-mitochondrial respiration (Non-mito), and proton leak were compared between the two groups using Student's t-test (n=8 mice per group).

Additionally, the distribution pattern of mitochondria was influenced by LD content. In contrast to their preferential cytosolic localization (cytosolic mitochondria) in LD^{high} macrophages, mitochondria co-localized with LDs, resembling peri-droplet mitochondria (PDM)[73,74], primarily in LD^{inter} macrophages (Fig. 13A, B). Cytosolic mitochondria and PDMs are supposed to have opposite functions in LD metabolism[73]. Notably, Dicer knockout increased the proportion of LD^{inter} and LD^{high} macrophages with PDMs (Fig. 13A, B). These results indicate that Dicer limits LD formation by redistributing mitochondria from a peri-droplet to cytosolic localization.

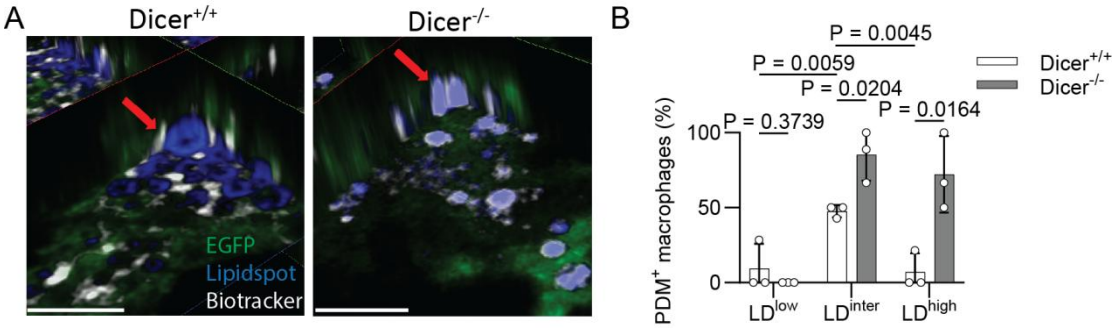

Fig. 13: Dicer knockout affected mitochondrial distribution in plaque macrophages

(A) Live plaque imaging was performed on aortic arch tissues with plaques from $Apoe^{-/-}$mTmG/LysMCre$^{T/T}$/Dicer$^{flox/flox}$ and $Apoe^{-/-}$mTmG/LysMCre$^{T/T}$/Dicer$^{WT/WT}$ mice, with LDs stained by lipidspot and mitochondria by BioTracker 405 Blue Mitochondria (Biotracker). Cross-sectional views of a 3D reconstruction are shown. Scale bars: 5 µm. (B) The fraction of macrophages containing PDMs was compared between $Apoe^{-/-}$mTmG/LysMCre$^{T/T}$/Dicer$^{flox/flox}$ ($Dicer^{-/-}$) and $Apoe^{-/-}$mTmG/LysMCre$^{T/T}$/Dicer$^{WT/WT}$ ($Dicer^{+/+}$) mice. The percentage of PDM^{+} macrophages in each subtype was compared between genotypes using Student's t-test. Comparisons among subtypes within the genotype were performed using one-way ANOVA with Fisher's LSD test (n = 3 mice per group).

3.4 Effect of Dicer on macrophage apoptosis and secondary necrosis in plaques

Because mitochondrial dysfunction may lead to cell death, I investigated caspase-3 activity in plaque macrophages using the NucView® 405 Caspase-3 dye, which stains DNA upon cleavage by caspase-3. I detected caspase 3 activation in 30% of the LD^{high}, 20% of LD^{inter}, but not in LD^{low} macrophages (Fig. 14A, B). Dicer knockout increased caspase 3 activation in LD^{high} but not in LD^{low} and LD^{inter} macrophages (Fig. 14A, B). Notably, in some LD^{high} macrophages, the cytosol was stained by the caspase 3 activated DNA dye (C3D) together with nuclear DNA, indicating the presence of

cytosolic DNA (Fig. 14A). Moreover, knockout of Dicer led to an increase of LD^{high} macrophages with cytosolic DNA stained by C3D (Fig. 14C). Using a mitochondrial membrane potential-dependent mitochondria dye (Mitoview 633), I observed that C3D^{+} cytosolic DNA appeared at sites next to mitochondria that lost their membrane potential (Fig. 14D), indicating the cytosolic DNA was likely mtDNA released from dysfunctional mitochondria. Taken together, Dicer inhibited caspase 3 activation in response to mtDNA release in LDhigh macrophages.

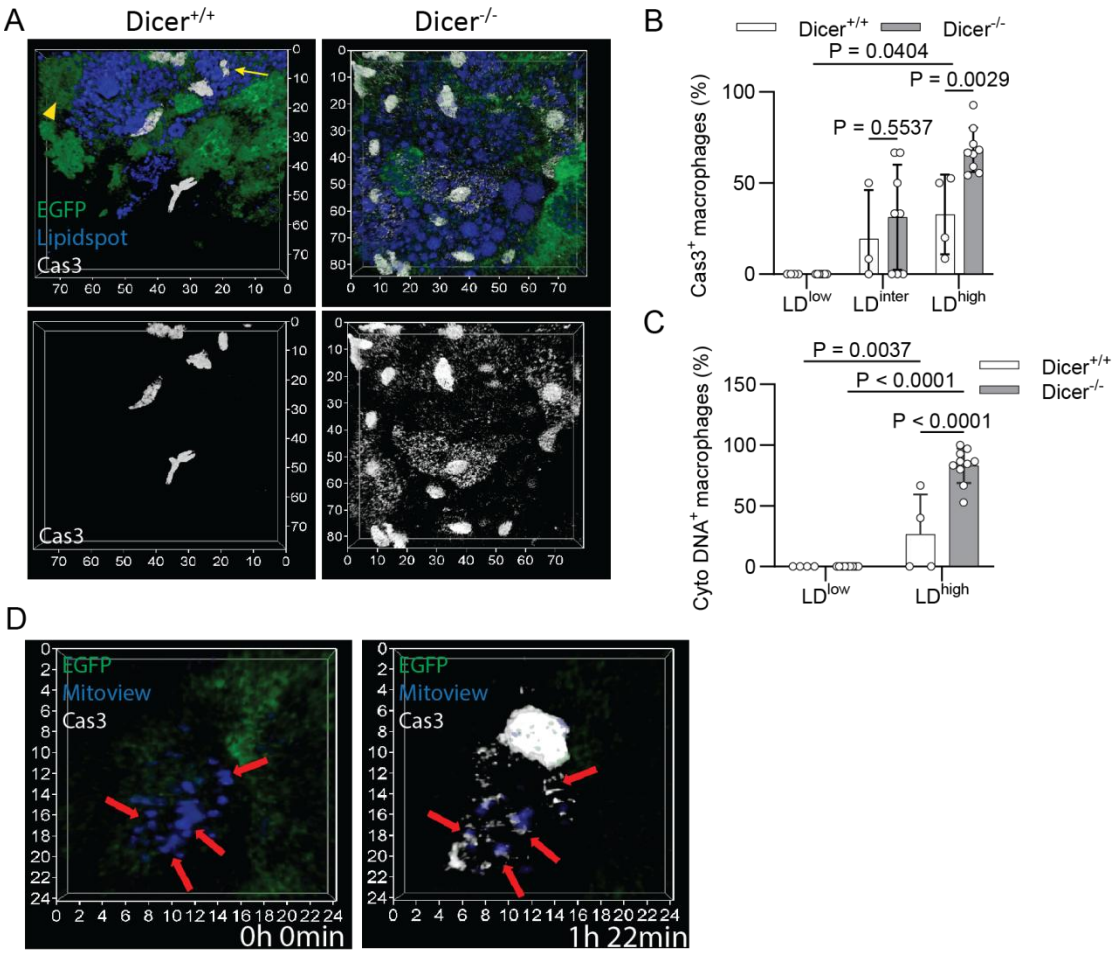

Fig. 14: Dicer knockout increased caspase 3 activation in LD^{high} macrophage

Live plaque imaging was performed on aortic arch tissues with plaques from Apoe$^{-/-}$mTmG/LysMCre$^{T/T}$/Dicer$^{flox/flox}$ (Dicer$^{-/-}$) and Apoe$^{-/-}$mTmG/LysMCre$^{T/T}$/Dicer$^{WT/WT}$ (Dicer$^{+/+}$) mice. 3D views are shown. (A) Representative images of C3D staining in plaques. The arrow indicates LD^{high} macrophage, and the arrowhead indicates LD^{low} macrophage. Lesional macrophage apoptosis (B) and macrophage with cytosolic DNA distribution (C) were determined by C3D staining for Apoe$^{-/-}$mTmG/LysMCre$^{T/T}$/Dicer$^{flox/flox}$ (Dicer$^{-/-}$) and Apoe$^{-/-}$mTmG/LysMCre$^{T/T}$/Dicer$^{WT/WT}$ (Dicer$^{+/+}$) mice. The percentage of Cas3^{+} macrophages in each subtype was compared between genotypes using Student's t-test. Comparisons among the three subtypes within the genotype were performed using one-way ANOVA with Fisher's LSD test (B, n = 4-9 mice per group). The percentage of cytosolic DNA^{+}

macrophages was compared with Student's t-test (C, n = 4-10 mice per group). (D) Caspase 3 activity and mitochondrial activity in plaque macrophages were visualized within one hour and 22 minutes. Arrows indicate sites where the Mitoview signal diminished and a caspase-3-activated DNA signal appeared.

Notably, I observed that some C3D^{+} LD^{high} macrophages with a cytosolic DNA distribution lost their membrane signal after caspase 3 activation, suggesting that these cells underwent secondary necrosis (Fig. 15). The loss of membrane signal suggests that their cellular contents, such as DNA, were exposed to the extracellular space.

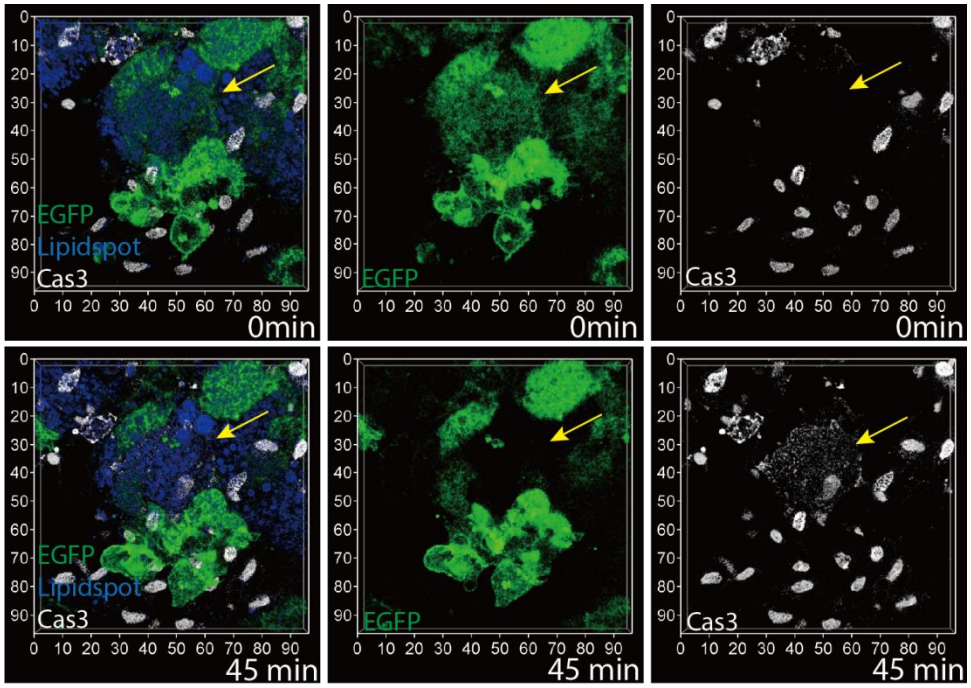

Fig. 15: Macrophage with C3D^{+} cytosolic DNA underwent secondary necrosis

Live plaque imaging was performed for an aortic arch tissue with plaques from a Apoe$^{-/-}$mTmG/LysMCre$^{T/T}$/Dicer$^{flox/flox}$ mouse. A 3D view is shown. Time of imaging is indicated. Arrows indicate an LD^{high} macrophage showing caspase 3 activation and cytosolic DNA distribution, followed by membrane loss.

Next, I investigated Dicer's role in regulating the secondary necrosis of apoptotic macrophages by assessing the extracellular Cas3+ DNA levels. I discovered that the absence of Dicer resulted in a higher volume of extracellular DNA in the plaque (Fig. 16), suggesting that Dicer plays a protective role against secondary necrosis, thereby

reducing DNA exposure to the extracellular environment. Interestingly, some of the extracellular DNA exhibited a tubular structure (Fig. 16).

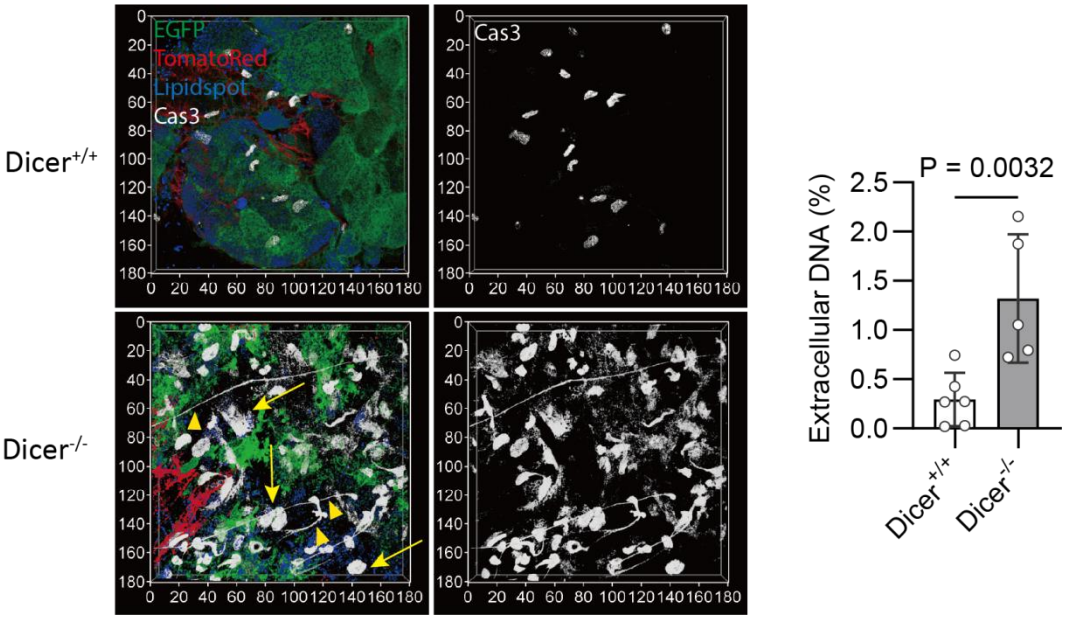

Fig. 16: Dicer knockout increased extracellular DNA accumulation in the plaque

Live plaque imaging was performed on aortic arch tissues with plaques from Apoe$^{-/-}$mTmG/LysMCre$^{T/T}$/Dicer$^{flox/flox}$ (Dicer$^{-/-}$) and Apoe$^{-/-}$mTmG/LysMCre$^{T/T}$/Dicer$^{WT/WT}$ (Dicer$^{+/+}$) mice. A 3D view is shown. Arrows indicate extracellular DNA, and arrowheads indicate extracellular DNA with a tube-like morphology. Extracellular DNA was quantified as C3D^{+} DNA volume not co-localized with EGFP and TomatoRed, normalized to the total imaging volume in the plaque, and compared between Apoe$^{-/-}$mTmG/LysMCre$^{T/T}$/Dicer$^{flox/flox}$ (Dicer$^{-/-}$) and Apoe$^{-/-}$mTmG/LysMCre$^{T/T}$/Dicer$^{WT/WT}$ (Dicer$^{+/+}$) mice using Student's t-test (n=5-6 mice per group).

3.5 Effect of Dicer on crystal formation in the plaque

Apoptosis and secondary necrosis of LD-containing macrophages are associated with the formation of CCs in plaques. Therefore, crystal deposition in the plaque was checked using reflection microscopy during live plaque imaging. Notably, I observed extracellular crystals formed at the surface of extracellular Cas3+ DNA (Fig. 17A, B), suggesting that extracellular Cas3+ DNA may serve as a nucleation site for crystallization. Moreover, I observed the co-localization of needle-like crystals with membrane debris and mitochondria (Fig. 17C). These results indicate that cellular contents released after necrosis contribute to CC formation.

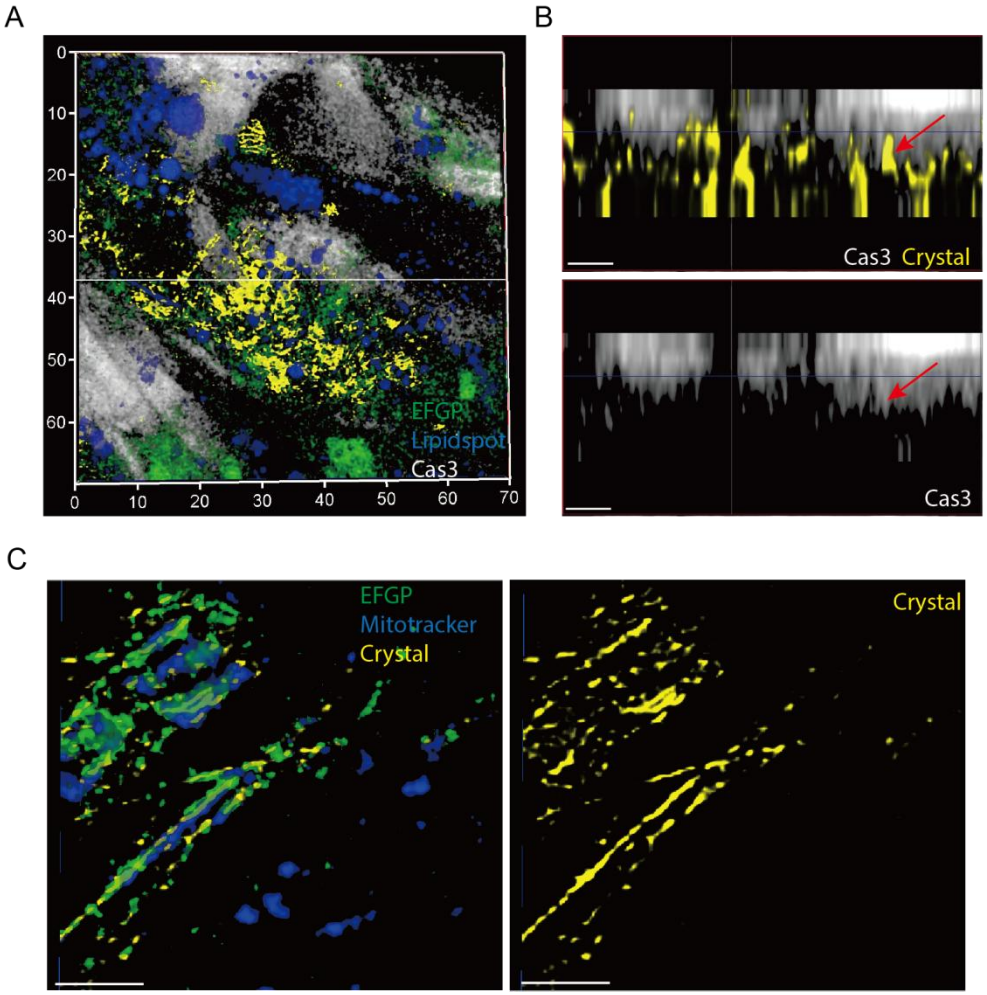

Fig. 17: Crystal deposition in the plaque

Live plaque imaging was performed on aortic arch tissues with plaques from Apoe$^{-/-}$mTmG/LysMCre$^{T/T}$/Dicer$^{flox/flox}$ and Apoe$^{-/-}$mTmG/LysMCre$^{T/T}$/Dicer$^{WT/WT}$ mice. Crystals were visualized by reflection confocal microscopy. Section views are shown. (A) Representative image of crystals co-localized with extracellular DNA. (B) Cross-section view of (A) to demonstrate the co-localization of DNA and crystal, indicated by arrows. Scale bars: 5 µm. (C) Representative image of crystals co-localized with membrane debris (EGFP) and mitochondria (Mitotracker). Scale bars: 5 µm.

To evaluate Dicer's effect on plaque crystal formation, polarized light microscopy was used to detect crystals in en face-prepared aortas following Oil Red O staining. The plaque crystal area increased after Dicer knockout (Fig. 18 A-C), suggesting Dicer limits plaque crystal formation by preventing the accumulation of extracellular DNA following secondary necrosis.

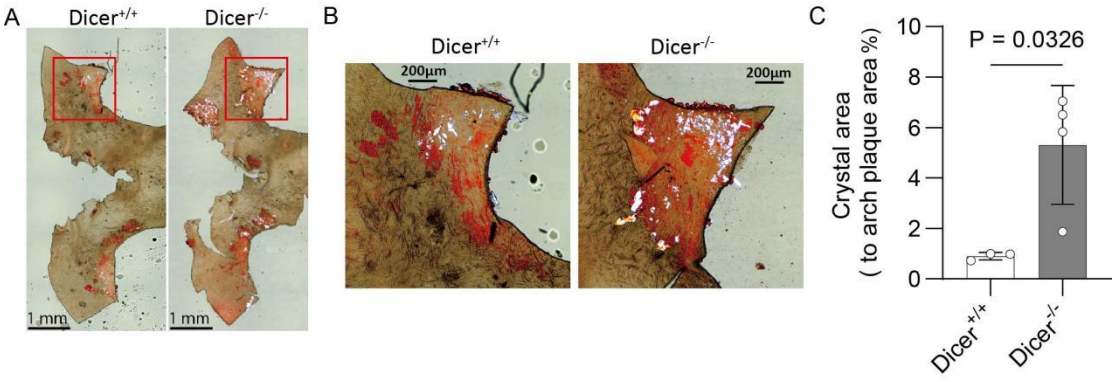

Fig. 18: Dicer knockout promoted crystal formation in the plaque

CCs were studied in oil red-O-stained, en face prepared aortas from Apoe$^{-/-}$/LysMCre$^{T/T}$/Dicer$^{flox/flox}$ (Dicer$^{-/-}$) and Apoe$^{-/-}$/LysMCre$^{T/T}$/Dicer$^{WT/WT}$ (Dicer$^{+/+}$) mice by polarized light microscopy. Red is oil red-O signals, and white is crystal signals. (A) Representative images of crystals in oil red-O-stained aortic arch. (B) Magnified view of the region outlined by the red squares from (A). (C) Crystal area in the plaque area (identified by oil red-O positive area) was compared between Apoe$^{-/-}$/LysMCre$^{T/T}$/Dicer$^{flox/flox}$ (Dicer$^{-/-}$) and Apoe$^{-/-}$/LysMCre$^{T/T}$/Dicer$^{WT/WT}$ (Dicer$^{+/+}$) mice using Student's t-test (n=3-4 mice per group).

3.6 Distinct effects of Dicer on interferon signaling in macrophage subtypes

LD-containing and inflammatory macrophages constitute two main subtypes in the plaque[37,38]. To investigate the effect of Dicer on LD-containing and inflammatory macrophages, proteomic analysis of oxLDL or LPS/IFN-γ-treated BMDMs from Apoe$^{-/-}$/LysMCre$^{T/T}$/Dicer$^{flox/flox}$ and Apoe$^{-/-}$/LysMCre$^{T/T}$/Dicer$^{WT/WT}$ mice was performed. LPS/IFN-γ treatment in BMDMs from the Apoe$^{-/-}$/LysMCre$^{T/T}$/Dicer$^{WT/WT}$ mice up-regulated proteins involved in immune and interferon response, such as STAT1, STAT2, ISG15, and IFIT3, while oxLDL treatment up-regulated proteins related to lipid metabolism like CD36 and ACBA1 (Fig. 19A). Consistently, the defense response to viruses, the response to type I interferon, the response to lipopolysaccharides, and the response to lipids were the most significantly enriched pathways identified by g:Profiler (Fig. 19B).

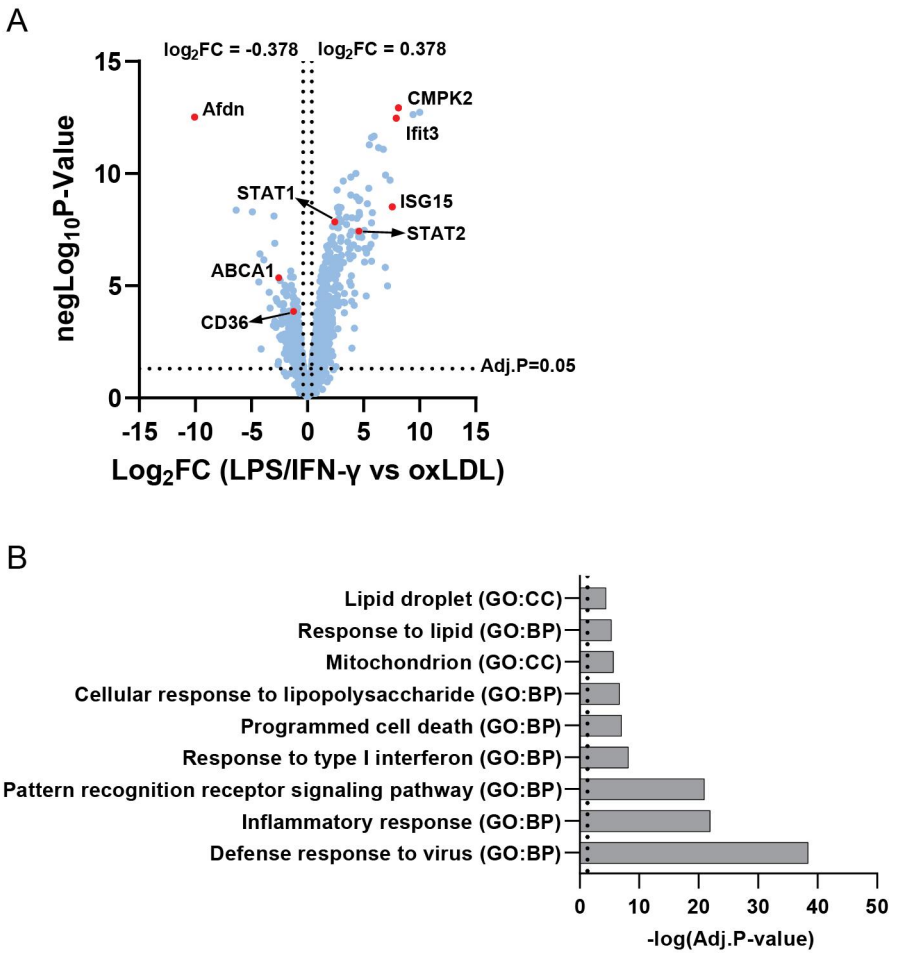

Fig. 19: Proteomic comparison between inflammatory and LD-containing macrophages

(A) Proteomic analysis of oxLDL-treated and LPS/IFN-γ-treated BMDMs from Apoe$^{-/-}$/LysMCre$^{T/T}$/Dicer$^{WT/WT}$ mice (n=5 per group, Limma-test), shown by volcano plot. (B) Pathway analysis for differentially expressed proteins (DEPs) between oxLDL-treated and LPS/IFN-γ-treated BMDMs from Apoe$^{-/-}$/LysMCre$^{T/T}$/Dicer$^{WT/WT}$ mice, identified by using *g: Profiler*.

In oxLDL-treated macrophages, Dicer knockout up-regulated 456 and down-regulated 538 out of 3809 studied proteins [adj. P< 0.05, absolute fold change (FC) > 1.3] (Fig. 20A). In LPS/IFN- γ-treated macrophages, 394 out of 3805 detected proteins were up-regulated and 318 were down-regulated by knockout of Dicer (Fig. 20B, adj. P< 0.05, absolute FC > 1.3). Notably, Dicer knockout regulated only 22 proteins in the same direction in oxLDL-treated and LPS/IFN-γ-treated BMDMs, with 10 proteins up-regulated, such as Hmox1, and 12 down-regulated, such as Myl6.

Next, we conducted pathway analysis for DEPs using Ingenuity Pathway Analysis (IPA). In oxLDL-treated macrophages, Dicer knockout most strongly enriched and activated the interferon signaling pathway (Fig. 20C). Key regulators of interferon pathway, such as STAT1 and STAT2, and the interferon-stimulated proteins like

ISG15, and IFIT3, were up-regulated after Dicer knockout (Fig. 20A). However, in LPS/IFN-γ-treated macrophages, the interferon signaling pathway was inhibited (Fig. 20D), with pathway-related proteins such as STAT2 and IFIT3 down-regulated following Dicer knockout (Fig. 20B). Notably, the degradation of chondroitin sulfate was the most enriched and inhibited pathway after Dicer knockout in LPS/IFN-γ-treated macrophages. (Fig. 20D). These findings suggest that Dicer plays distinct and even opposing roles in oxLDL- and LPS/IFN-γ treated macrophages concerning the interferon response.

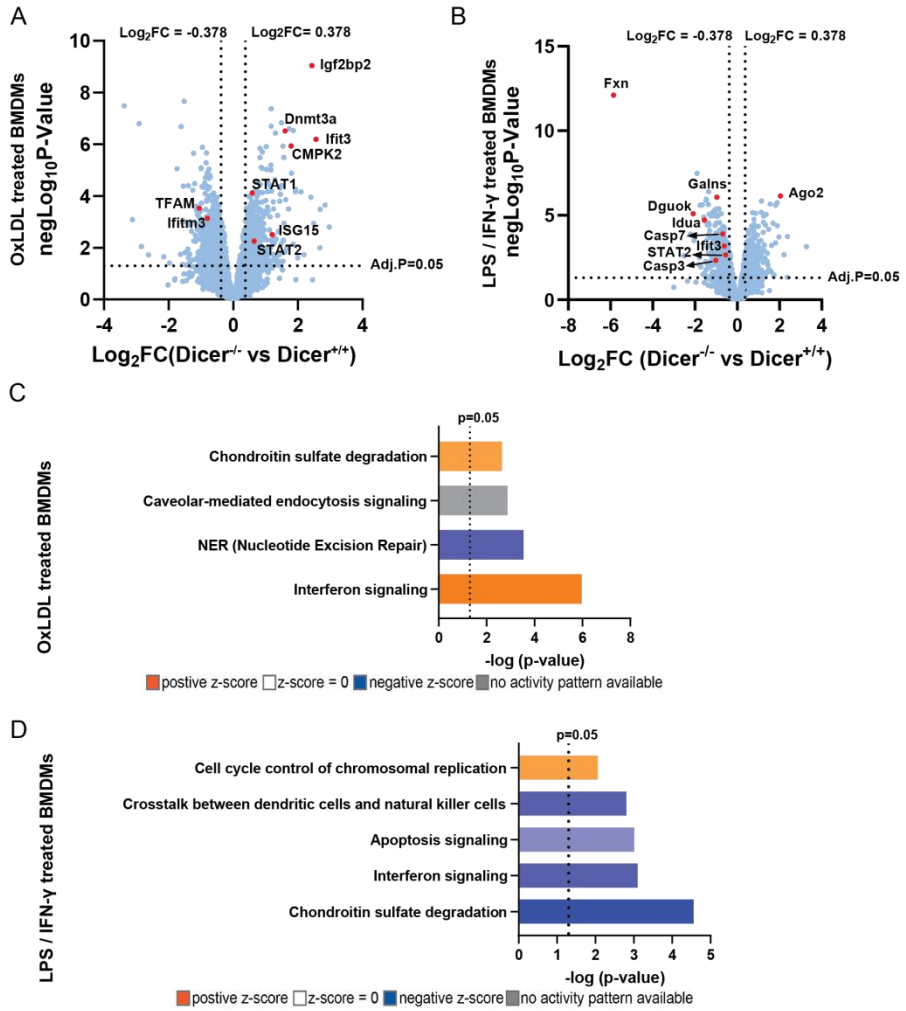

Fig. 20: Differential effect of Dicer knockout on interferon signaling in macrophage subtypes

(A and B) Proteomic analysis of oxLDL-treated (A) and LPS/IFN-γ-treated (B) BMDMs from Apoe$^{-/-}$/LysMCre$^{T/T}$/Dicer$^{flox/flox}$ (Dicer$^{-/-}$) and Apoe$^{-/-}$/LysMCre$^{T/T}$/Dicer$^{WT/WT}$ (Dicer$^{+/+}$) mice (n=5 per group, limma-test), shown by volcano plot. (C and D) Ingenuity Pathway Analysis for DEPs in oxLDL-treated (A) and LPS/IFN-γ-treated (B) BMDMs between Apoe$^{-/-}$/LysMCre$^{T/T}$/Dicer$^{flox/flox}$ (Dicer$^{-/-}$) and Apoe$^{-/-}$/LysMCre$^{T/T}$/Dicer$^{WT/WT}$ (Dicer$^{+/+}$) mice, positive z-score and negative z-score indicate the pathway is activated and inhibited, respectively.

Release of mtDNA into the cytosol has been reported to induce the pSTAT1-dependent Type I interferon response[75,76]. Given the observation of cytosolic DNA distribution in LD^{high} macrophages, I hypothesized that Dicer knockout triggers interferon signaling by promoting mtDNA release in LD-containing macrophages. To verify the hypothesis, I checked the cytosolic mtDNA accumulation by measuring the cytosolic level of cytochrome c oxidase I DNA using PCR to determine the mtDNA release. Accordingly, Dicer knockout increased cytosolic cytochrome c oxidase I level in oxLDL-treated macrophages (Fig. 21A), indicating that Dicer plays a role in LD-mediated mtDNA release. Moreover, Dicer knockout increased the protein level of phosphorylated STAT1 (pSTAT1) detected by JESS (Fig. 21B). Taken together, Dicer limits mtDNA release and pSTAT1-mediated activation of interferon signaling in LD-containing macrophages.

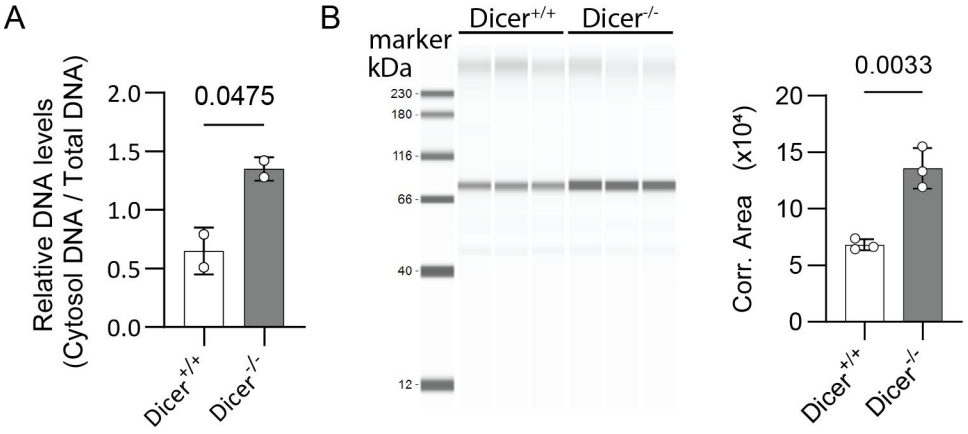

Fig. 21: Dicer knockout promoted mtDNA release and type I interferon signaling pathway activation in LD-containing macrophages

(A) Quantitation of mtDNA Cytochrome c oxidase I DNA level in the cytosol of oxLDL-treated BMDMs from Apoe$^{-/-}$/LysMCre$^{T/T}$/Dicer$^{flox/flox}$ (Dicer$^{-/-}$) and Apoe$^{-/-}$/LysMCre$^{T/T}$/Dicer$^{WT/WT}$ (Dicer$^{+/+}$) mice (n=2). Student's t-test was used to compare the groups. (B) Quantitation of pSTAT1 protein expression in oxLDL-treated BMDMs from Apoe$^{-/-}$/LysMCre$^{T/T}$/Dicer$^{flox/flox}$ (Dicer$^{-/-}$) and Apoe$^{-/-}$/LysMCre$^{T/T}$/Dicer$^{WT/WT}$ (Dicer$^{+/+}$) mice [detected by Jess, normalized to the total protein (PN), n=3]. The blot of three replicates is shown. Student's t-test was used to compare the groups.

3.7 Targets of miRNAs generated by Dicer in macrophages

Dicer controls the maturation and expression of almost all miRNAs[65]. Therefore, I investigated the effect of Dicer knockout on miRNA targeting in macrophages. To this end, I conducted tAGO2-GFP IP using aortic tissue and BMDMs in

$Apoe^{-/-}$/$tAgo2^{T/T}$/$LysMCre^{T/T}$/$Dicer^{flox/flox}$ and $Apoe^{-/-}$/$tAgo2^{T/T}$/$LysMCre^{T/T}$/$Dicer^{WT/WT}$ mice expressing tAGO2 proteins specifically in myeloid cells. The tAGO2 protein was detected using a GFP antibody in the after IP samples but not in the before IP samples, confirming its specific enrichment after IP (Fig. 22A). Subsequently, IP samples were used to perform the prime-sequencing and compared the mRNA abundance in the IP samples between $Apoe^{-/-}$/$tAgo2^{T/T}$/$LysMCre^{T/T}$/$Dicer^{flox/flox}$ and $Apoe^{-/-}$/$tAgo2^{T/T}$/$LysMCre^{T/T}$/$Dicer^{WT/WT}$ mice. In BMDMs, the enrichment analysis revealed that Dicer knockout reduced the enrichment of 3956 out of 9769 genes detected in the RISC (Fig. 22B, $Log_2FC > 1$, q-value < 0.01). Among the 3956 genes, 484 and 306 mRNAs overlapped with the DEPs in oxLDL-treated and LPS/IFN-γ-treated BMDMs, respectively. In contrast to Dennd10, which is not regulated at protein levels, Hmox1, Itga5, and Mtap are among the most significantly enriched mRNAs and up-regulated by Dicer at protein levels in oxLDL- and/or LPS/IFN-γ-treated BMDMs (Fig. 22B and C).

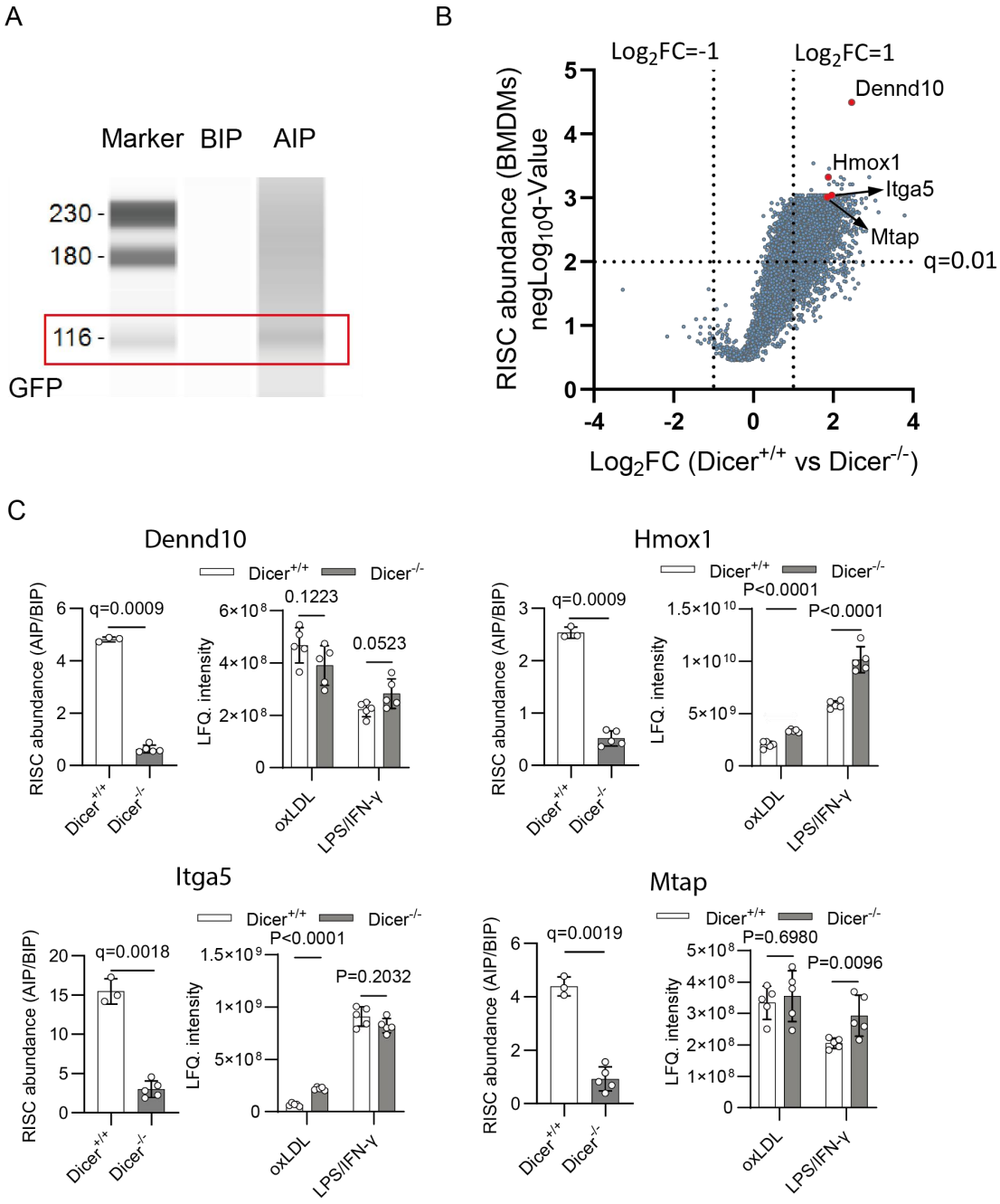

Fig. 22: Targets of Dicer-mediated miRNAs in BMDMs

(A) Detection of tAGO2 protein in before IP (BIP) sample and after IP (AIP) sample using GFP antibody by JESS automated western blot system. (B) Volcano plot of RISC abundance is identified as the ratio of AIP to BIP. Statistical analysis was performed using multiple *t*-tests with 1% FDR correction using the two-stage linear step-up procedure of Benjamini, Krieger, and Yekutieli. (C) RISC abundances (represented by the read count ratio of AIP to BIP) of the four genes most strongly enriched by Dicer in BMDMs from $Apoe^{-/-}/tAgo2^{T/T}/LysMCre^{T/T}/Dicer^{flox/flox}$ ($Dicer^{-/-}$) and $Apoe^{-/-}/tAgo2^{T/T}/LysMCre^{T/T}/Dicer^{WT/WT}$ ($Dicer^{+/+}$) mice and their protein levels in oxLDL-treated and LPS/IFN-γ-treated BMDMs from $Apoe^{-/-}/LysMCre^{T/T}/Dicer^{flox/flox}$ ($Dicer^{-/-}$) and

$Apoe^{-/-}$/$LysMCre^{T/T}$/$Dicer^{WT/WT}$ ($Dicer^{+/+}$). RISC abundance were compared between genotypes using multiple t-tests with a 1% FDR, controlled by the two-stage linear step-up procedure of Benjamini, Krieger, and Yekutieli, and in aortas using one-tailed multiple t-tests. Protein expression levels (LFQ. intensity) were compared between genotypes using Limma (ImShot v1.0.1).

In the atherosclerotic aorta, Dicer knockout in macrophages reduced 63 out of 178 detected mRNAs in the myeloid cell specific tAGO2-IP samples, such as Cathepsin B (Ctsb), Interferon Alpha Inducible Protein 27 Like 2 (Ifit27l2a) and Heat Shock Protein 90 Alpha Family Class B Member 1 (Hsp90ab1) (Fig. 23A).

Among the miRNA targets that showed reduced enrichment after Dicer knockout in plaque macrophages, 21 (33.3%) also showed reduction in BMDMs, including Vimentin (Vim), Ferritin Light Chain (Ftl1) and CD74 (Fig. 23B). In contrast, enrichment of targets like ISG15 and C3 were only reduced by Dicer knockout in plaque macrophages, suggesting they are athero specific targets (Fig. 23B).

Notably, among the identical targets between BMDMs and plaque macrophages, Ftl1 was the only one up-regulated at the protein level following Dicer knockout (Fig. 23C). Moreover, Dicer knockout increased Ftl1 expression in oxLDL-treated but not in LPS/IFN-γ-treated BMDMs (Fig. 23C), indicating that Dicer regulates Ftl1 specifically in LD-containing macrophages.

To confirm the effect of Dicer on Ftl1 expression, I examined Ftl1 levels in aortic root plaques with immunofluorescence staining. Consistently, Dicer knockout increases Ftl1 expression in plaque macrophages from the aortic root (Fig. 23D). Taken together, these results indicate Dicer inhibits Ftl1 expression in LD-containing macrophages by producing miRNAs.

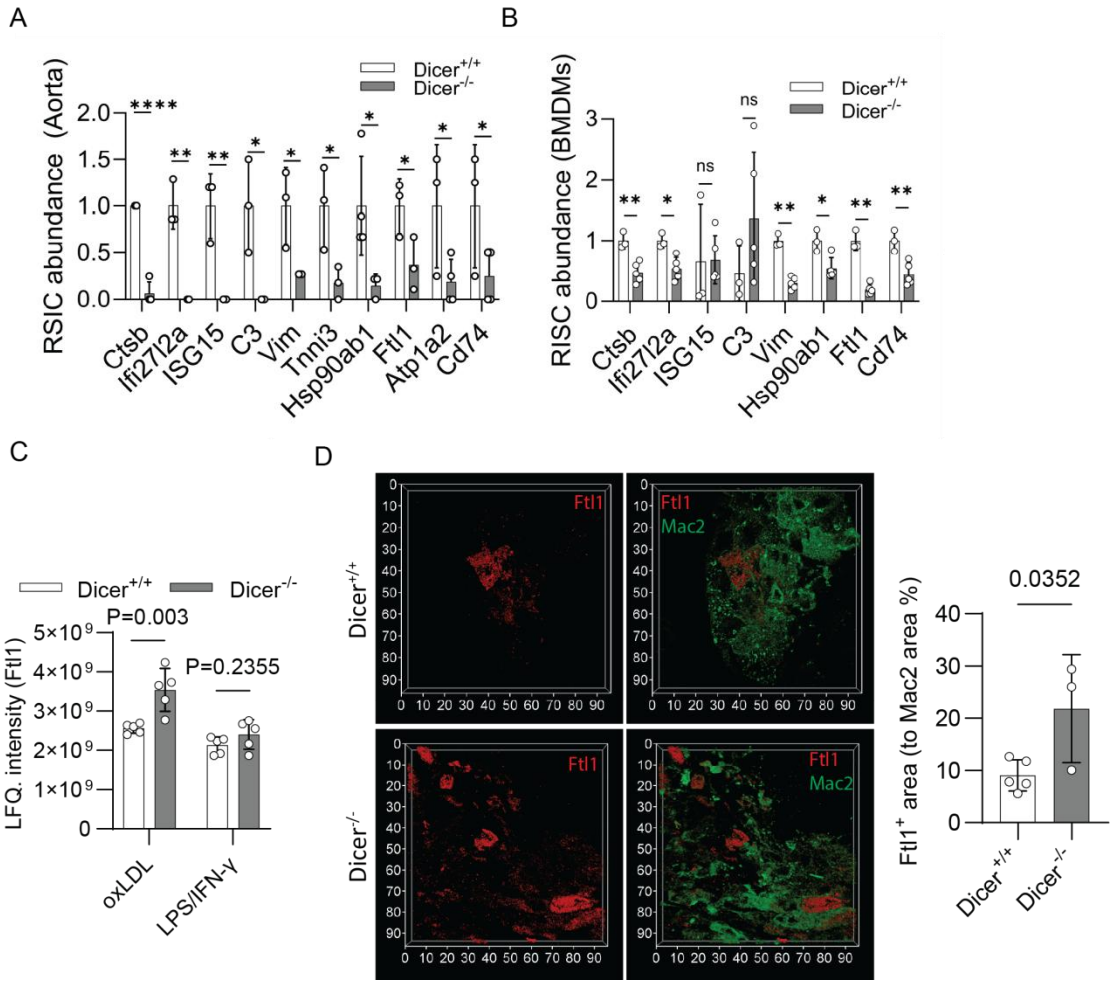

Fig. 23: Dicer knockout reduced Ftl1 targeting in LD-containing macrophages

(A) The ten mRNAs most strongly reduced in the Dicer knockout from the tAgo2 IP in aorta tissue after 12 weeks of a high-fat diet. The mRNA abundance was quantified as AIP read counts in the $Apoe^{-/-}/tAgo2^{T/T}/LysMCre^{T/T}/Dicer^{flox/flox}$ ($Dicer^{-/-}$) mice group, normalized to the $Apoe^{-/-}/tAgo2^{T/T}/LysMCre^{T/T}/Dicer^{WT/WT}$ ($Dicer^{+/+}$) mice group. Statistical comparisons were performed using one-tailed multiple *t*-tests. (n=3-4 mice in each group). *p<0.05, ** p<0.01, **** p<0.0001. (B) The abundance of mRNAs from (A) in the RISC from BMDMs. The mRNA abundance was quantified as read counts ratio of AIP to BIP in the $Apoe^{-/-}/tAgo2^{T/T}/LysMCre^{T/T}/Dicer^{flox/flox}$ ($Dicer^{-/-}$) mice group, normalized to the $Apoe^{-/-}/tAgo2^{T/T}/LysMCre^{T/T}/Dicer^{WT/WT}$ ($Dicer^{+/+}$) mice group. Statistical comparisons were performed using multiple *t*-tests with 1% FDR correction using the two-stage linear step-up procedure of Benjamini, Krieger, and Yekutieli (n=3-5 per group). *q<0.05, ** q<0.01. (C) Comparison of Ftl1 protein expression levels in oxLDL-treated and LPS/IFN-γ-treated BMDMs between $Apoe^{-/-}/LysMCre^{T/T}/Dicer^{flox/flox}$ ($Dicer^{-/-}$) and $Apoe^{-/-}/LysMCre^{T/T}/Dicer^{WT/WT}$ ($Dicer^{+/+}$) mice. (D) Comparison of Ftl1 protein levels in plaque macrophages from the aortic root of $Apoe^{-/-}/LysMCre^{T/T}/Dicer^{flox/flox}$ ($Dicer^{-/-}$) and $Apoe^{-/-}/LysMCre^{T/T}/Dicer^{WT/WT}$ ($Dicer^{+/+}$) mice, quantified as $Ftl1^{+}$ area to $Mac2^{+}$ area. Statistical analysis was performed using Student's t-test (n=3-5 mice per group).

3.8 Regulation of miRNA expression by Dicer in LD-containing macrophages

Next, I investigated which miRNAs are regulated by Dicer in LD-containing macrophages by conducting miRNA profiling using nanostring nCounter expression panel in oxLDL-treated BMDMs from Apoe$^{-/-}$/LysMCre$^{T/T}$/Dicer$^{flox/flox}$ and Apoe$^{-/-}$/LysMCre$^{T/T}$/Dicer$^{WT/WT}$ mice. In oxLDL-treated BMDMs from Apoe$^{-/-}$/LysMCre$^{T/T}$/Dicer$^{WT/WT}$ mice, 10 miRNAs, such as miR-16, let-7d, and miR-27a, together represented almost 50% of the total pool of 566 miRNAs (Fig. 24A). Notably, Dicer knockout reduced the expression of 79 miRNAs (Fig. 24B, adj. P < 0.05, absolute FC > 2), including 9 of these most abundant miRNAs, except miR-1224.

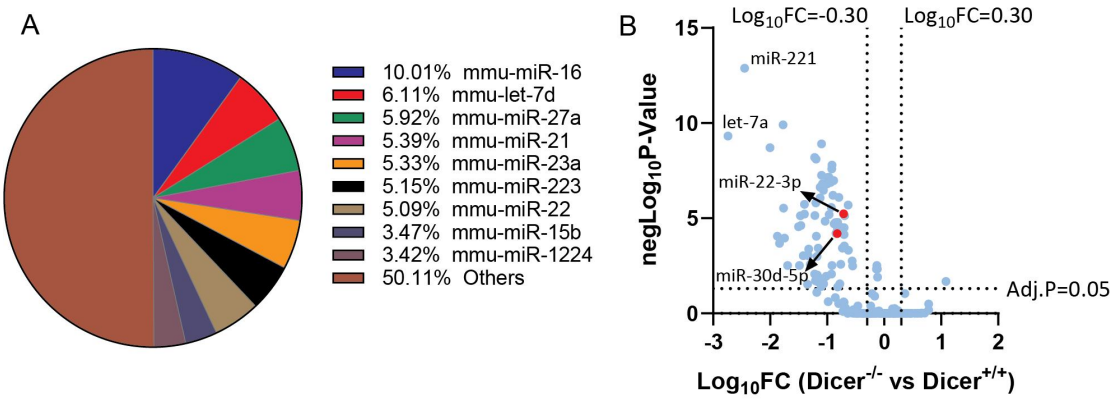

Fig. 24: The regulation of miRNA expression by Dicer in LD-containing macrophages

(A) The top 10 most abundant miRNAs in oxLDL-treated BMDMs from Apoe$^{-/-}$/LysMCre$^{T/T}$/Dicer$^{WT/WT}$ mice were shown as percentages of the total miRNA pool in a pie chart. (B) Volcano plot of differentially expressed miRNAs between oxLDL-treated BMDMs from Apoe$^{-/-}$/LysMCre$^{T/T}$/Dicer$^{flox/flox}$ (Dicer$^{-/-}$) and Apoe$^{-/-}$/LysMCre$^{T/T}$/Dicer$^{WT/WT}$ (Dicer$^{+/+}$) mice, compared using multiple *t*-test with Holm-Šídák correction (n=6 per group).

Among the most abundant and down-regulated miRNAs by Dicer knockout, miR-22-3p has a predicted binding site within the 3'-UTR of Ftl1 mRNA, identified by both *RNAhybrid* (Fig. 25A) and *Targetscan* (Fig. 25B). Moreover, this binding site is conserved between mouse and human (Fig. 25C). These findings suggest that miR-22-3p mediates the repression of Ftl1 by Dicer in LD-containing macrophages. Notably, the miR-30 family, which is also down-regulated by Dicer knockout (Fig.

24B), has conserved binding sites within the 3'-UTR of Vim mRNA (Fig. 25D and E), suggesting a role of Dicer-mediated miR-30 in Vim targeting.

A

```
target: Ftl1-201
length: 163
miRNA : mmu-miR-22-3p
length: 22

mfe: -22.5 kcal/mol
p-value: undefined

position  77
target 5'      C       AGCC    A         U 3'
                UCU CA     ACU GGCAGCUU
                AGA GU     UGA CCGUCGAA
miRNA  3' UGUCA    A                    5'
```

B

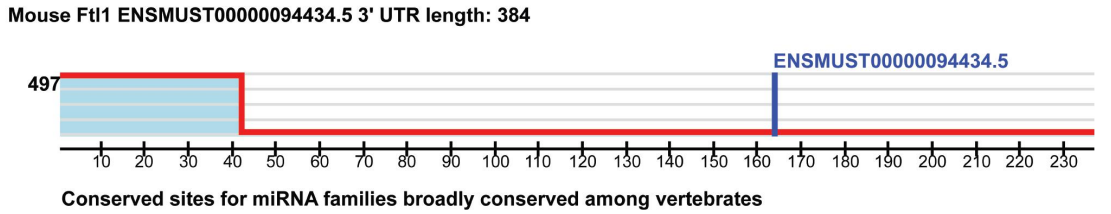

C

D

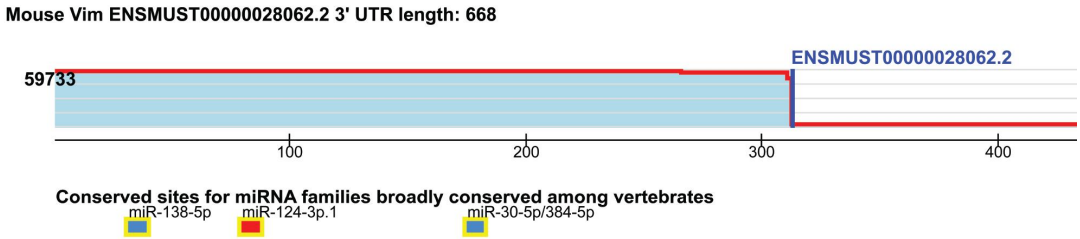

E

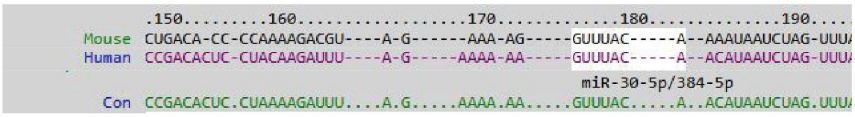

Fig. 25: Predicted targets of Dicer-regulated miRNAs in LD-containing macrophages

(A and B) Binding site prediction for Ftl1 3'-UTR and miR-22-3p was performed using RNAhybrid (A) and TargetScan (B). (C) TargetScan identified the conservation of the miR-22-3p binding site within the Ftl1 3'-UTR between mouse and human. (D) Binding site prediction for Vim 3'-UTR and miR-30-5p was conducted using TargetScan. (E) TargetScan identified the conservation of the miR-30-5p binding site within the Vim 3'-UTR between mouse and human.

4. Discussion

4.1 Role of Dicer in LD accumulation in plaque macrophages

Here, I identified three subtypes of plaque macrophages that differ in their LD content: LD^{high}, LD^{inter}, and LD^{low} macrophages. Dicer expression in macrophages limits the formation of LD^{high} macrophages while increasing LD^{low} macrophages in the plaque. This suggests that these macrophage subtypes represent dynamic and interrelated phenotypic states rather than independent subsets, with LD^{low} macrophages potentially transitioning into LD^{high} macrophages, a process inhibited by Dicer. Moreover, Dicer's effect on limiting LD^{high} macrophage formation is due to a restriction in LD growth (Fig. 26).

Mitochondrial subpopulations with distinct distribution patterns regulate LD sizes. Unlike cytosolic mitochondria, which restrict the expansion of LDs through fatty acid beta oxidation, PDMs facilitate LD expansion by supplying ATP from enhanced pyruvate oxidation for triglyceride synthesis [74]. Although PDMs have been found in cells or tissues, such as brown adipocytes, hepatocytes, cardiomyocytes, and skeletal muscle fibers[74,77-80], they have not been previously reported in LD-containing macrophages. Notably, I observed PDMs primarily in LD^{inter} macrophages, in contrast to the cytosolic distribution of mitochondria found in LD^{high} and LD^{low} macrophages. This observation suggests a transient relocation of cytosolic mitochondria to form PDM in LD^{inter} macrophages, supporting LD growth during the transition from LD^{low} to LD^{high} macrophages. Following LD^{high} macrophage formation, PDMs are reduced, potentially to prevent excessive LD accumulation. Moreover, I found Dicer promotes the reduction of PDMs in LD^{high} and LD^{inter} macrophages, which underlie its role in restricting LD growth and limiting LD^{high} macrophage formation (Fig. 26).

Since PDM formation necessitates contact between mitochondria and LDs[73], it is suggested that Dicer initiates the separation of PDMs from LDs during the transformation into LD^{high} cells. The influence of Dicer on LD-mitochondria contacts prompted us to consider the potential mechanisms regulating this interaction. Notably, LDs and mitochondria are attached to intermediate filaments[81,82]. I found that Dicer regulates Vimentin (Vim), a key intermediate filament cytoskeleton protein, by targeting it with miRNAs, as the enrichment of Vim was decreased in the RISC following Dicer knockout in plaque macrophages. Notably, Vim, which is also found on the LD membrane[83], regulates the interaction between LDs and mitochondria through cytoskeletal reorganization[82]. Moreover, the 3'-UTR of Vim contains highly conserved binding sites for miRNAs from the miR-30 family[84], which were reduced in the absence of Dicer in oxLDL-treated BMDMs. Therefore, this

finding suggest that Dicer controls PDM abundance by miRNAs-mediated regulation of LD-mitochondria contacts during LD^{high} macrophage formation through targeting Vim (Fig. 26). Nevertheless, further experiments are required to validate this hypothesis.

Notably, Ftl1, which encodes the ferritin light chain protein, is another Dicer-regulated target of miRNAs in plaque macrophages and oxLDL-treated BMDMs. Accordingly, I observed that Dicer knockout up-regulated Ftl1 in plaque macrophages. Ftl1, together with the ferritin heavy chain, forms ferritin, the iron storage protein in cells that regulates the availability of free iron[85]. The cellular iron homeostasis influences LD formation and the formation of contacts between LDs and mitochondria[86], indicating that Ftl1 may play a role in PDM formation. Interestingly, the short 3'UTR of Ftl1 contains a conserved binding site for miR-22-3p. Since Dicer knockout decreased miR-22-3p expression in oxLDL-treated BMDMs, I hypothesize that the regulation of the iron homeostasis in plaque macrophages by miR-22-regulated Ftl1 may be involved in the effect of Dicer on the abundance of PDMs (Fig. 26).

Alternatively, Dicer may also limit the uptake of oxLDL and thus the expansion of LDs in macrophages. However, results in this study show that the increased LD size in Dicer knockout macrophages was not associated with enhanced oxLDL uptake. Therefore, the increase in LD^{high} macrophages by Dicer knockout may not be due to the regulation of oxLDL uptake. Moreover, cholesterol efflux is unlikely to be involved in the Dicer effect on LD expansion, as the cholesterol content does not significantly contribute to LD size compared to triglycerides[87].

4.2 Role of Dicer in mitochondrial function of plaque macrophages

In LD^{high} macrophages, LD accumulation is associated with reduced mitochondrial activity. This finding contradicts the previous in vitro results, where lipid accumulation led to increased oxidative phosphorylation, similar to that in IL-4-stimulated macrophages[65]. This discrepancy highlights substantial differences between the in vivo and in vitro models regarding mitochondrial response to LD accumulation. Notably, a recent study reveals the heterogeneity of foam cells in human atherosclerosis. Whereas $TREM2^{+}$ foam cells exhibit high cholesterol metabolism and fatty acid degradation, $SPP1^{+}$ $TREM2^{-}$ foam cells show increased fatty acid biosynthesis and glycolysis, associated with cellular dysfunction and worse prognosis[88]. Consistently, the plaque LD^{high} macrophages I observed showed reduced mitochondrial respiration, a metabolic profile more closely resembling the $SPP1^{+}$

foam cell subtype. Dicer enhances mitochondrial activity in LD^{high} macrophages, consistent with previous in vitro findings[65]. These results suggest that although the mitochondrial response to LD accumulation differs between in vitro and in vivo conditions, the effect of Dicer on maintaining mitochondrial function was similar in both.

Lipid toxicity, such as free cholesterol overload, has been reported to cause mitochondrial dysfunction-induced apoptosis[14]. Despite this, this study suggest that Dicer may primarily limit the accumulation of TAG and LD, while the regulation of free cholesterol is uncertain. Notably, a previous study reported that excessive accumulation of TAG and LD in macrophages induces mitochondrial dysfunction, probably due to up-regulation of proapoptotic Bax, and the down-regulation of antiapoptotic bcl-2, leading to mitochondrial outer membrane permeabilization (MOMP) and intrinsic apoptosis[89]. This evidence aligns with my findings that enhanced formation of LDs after Dicer knockout is associated with a substantial reduction of mitochondrial function in LD^{high} macrophages. This suggests that Dicer may limit LD and TAG stress, thus preserving mitochondrial function (Fig. 26).

Additionally, Dicer-mediated Ftl1 may play a role in preventing mitochondrial dysfunction by maintaining iron homeostasis (Fig. 26). This is based on the fact that both iron overload and deficiency may induce mitochondrial dysfunction. Whereas iron overload induces mitochondrial dysfunction by oxidative stress, which is part of the ferroptosis pathway[90], iron deficiency is associated with impaired mitochondrial respiration in myocardium[91], probably due to the disrupted biosynthesis of Fe/S clusters, which are critical components of mitochondrial complexes I-V[92]. Nevertheless, further investigations are necessary to validate the hypothesis. Collectively, this evidence suggests that Dicer may enhance mitochondrial function in LD^{high} macrophages by regulating iron homeostasis and lipid accumulation.

4.3 Role of Dicer in macrophage apoptosis

In addition to regulating LD accumulation and mitochondrial function, Dicer protects macrophages against apoptosis in atherosclerotic plaques[65]. However, the underlying mechanism remains unclear. This study demonstrated that LD^{high}, rather than LD^{low}, is the primary source of caspase 3^{+} macrophages in atherosclerotic plaques. Notably, I found Dicer prevents LD^{high} macrophage caspase 3 activation, which is associated with the maintenance of mitochondrial function. Given that mitochondrial dysfunction can trigger the intrinsic apoptosis[93], this finding suggests that Dicer plays a protective role in preventing LD^{high} macrophage apoptosis,

probably by maintaining mitochondrial function (Fig. 26). Although Dicer knockout also reduced mitochondrial activity in LD^{low} macrophages, it did not lead to caspase 3 activation. This could be explained by the retaining mitochondrial activity in LD^{low} macrophages after Dicer knockout, which is sufficient to sustain cell survival, as compared to LD^{high} macrophages. Notably, the apoptosis pathway is inhibited by Dicer knockout in LPS/IFN-γ-treated BMDMs, which at least can partially explain the absence of caspase 3 activation in LD^{low} macrophages within the plaque after Dicer knockout. These findings support the hypothesis from previous study that Dicer's role in maintaining mitochondrial function may account for its protective effect against macrophage apoptosis in atherosclerotic plaques[65]. However, this effect is primarily observed in LD^{high} macrophages.

4.4 Role of Dicer in CC formation

4.4.1 Role of Dicer in extracellular DNA deposition

In caspase 3^+ LD^{high} macrophages, cytosolic DNA dye signals were detected. The appearance of these cytosolic DNA signals following mitochondrial membrane potential loss suggests that they are likely mtDNA. This aligns with prior research that mtDNA is released into the cytosol following mitochondrial dysfunction[93]. Notably, Dicer prevents cytosolic DNA distribution in LD^{high} macrophages. This is supported by the in vitro finding that Dicer knockout increased mtDNA release to the cytosol in LD-containing macrophages. These observations indicate that Dicer prevents mtDNA release into the cytosol after mitochondrial dysfunction in LD^{high} plaque macrophages (Fig. 26).

Notably, I observed caspase 3^+ LD^{high} macrophages undergoing secondary necrosis, characterized by membrane loss and exposure of DNA, primarily cytosolic DNA, to the extracellular space. In atherosclerotic plaques, apoptotic cells that are not promptly removed through efferocytosis eventually undergo secondary necrosis[22]. This aligns with my observation that efferocytosis is absent in the plaque. Notably, Dicer limits secondary necrosis and extracellular DNA distribution in the plaque (Fig. 26). This is likely attributed to its role in limiting LD^{high} macrophage apoptosis, thereby maintaining apoptosis-efferocytosis balance. Cell debris and intracellular content from secondary necrotic cells contribute to necrotic core formation[94]. Therefore, consistent with our previous finding, these results indicate that Dicer may limit necrotic core formation by preventing secondary necrosis of LD^{high} macrophages and the subsequent extracellular DNA deposition in the plaque.

4.4.2 Involvement of extracellular DNA in CC formation

Notably, I observed that some extracellular DNA in the plaque co-localized with crystals, suggesting a crystal-DNA association. This is supported by a previous study showing that DNA is present in the CC clot[95]. CC formation is triggered by a high level of free cholesterol accumulation, either spontaneously in the extracellular space or intracellularly[25-27]. Non-cholesterol substances or structures, such as amorphous components and LD membrane[96,97], facilitate heterogeneous cholesterol nucleation by serving as nucleation sites, probably more thermodynamically favorable than homogeneous nucleation occurring within the LD[97,98]. Thus, extracellular DNA may serve as a nucleation site, thereby promoting extracellular crystal formation and growth in the plaque. However, further investigation is required to reveal the role of extracellular DNA in crystal formation. Additionally, I found that some extracellular crystals with needle- or plate-like morphology are around LDs or co-localized with membrane debris. This aligns with previous studies showing that CCs can form on the LD membrane with a needle-like or thin-platy shape[25,99,100], or in cholesterol-rich plasma membrane with a plate-like shape[99]. Moreover, I observed crystals in the core region of the LDs from LD^{high} macrophages. The LD core has been previously shown to require higher cholesterol levels for crystal formation[97]. Thus, this finding suggests high cholesterol levels in the LDs of LD^{high} macrophages.

4.4.3 Dicer-mediated CC formation

Notably, Dicer prevents crystal formation in the plaque, probably functioning both intracellularly and extracellularly. The role of Dicer in limiting LD expansion in LD^{high} macrophages may restrict intracellular CC formation. Intracellular CC deposition in cells triggers multiple pathological effects, including lysosomal rupture by damaging lysosome membranes[101,102], mitochondrial dysfunction by inducing ROS[26], and inflammation by promoting NRLP3 inflammasome formation and IL-1 β secretion[103], ultimately leading to cell death[26,104]. Dicer may protect against this damage by limiting intracellular CC formation. Additionally, lysosomal protease Cathepsin B (Ctsb), one of the targets enriched in the RISC of plaque macrophages by Dicer, has been shown to be released into the cytosol following CC-induced lysosomal rupture[103]. This translocation of Ctsb into the cytosol is involved in CC-induced inflammation, NLRP3 activation, cell death[103,105-107]. Thus, Dicer may limit CC-induced cellular damage by regulating Ctsb. Accordingly, Dicer may limit intracellular CC-induced LD^{high} macrophage apoptosis and secondary necrosis, preventing the

release of DNA and cell debris, thereby mitigating extracellular CC accumulation (Fig. 26). Collectively, this research reveals a critical role of Dicer in limiting intracellular and extracellular CC formation in the plaque.

4.5 Role of Dicer in Type I interferon signaling in plaque macrophages

The cytosolic distribution of mtDNA, in addition to functioning in crystal formation extracellularly, can induce the Type I interferon response intracellularly[76]. Consistently, Dicer suppresses interferon signaling pathway activation in oxLDL but not LPS/IFN-γ-treated macrophages, as indicated by protein expression profile. Given the role of Dicer in limiting cytosolic DNA distribution in LD^{high} macrophages, Dicer may also restrict interferon response in plaque LD^{high} macrophages (Fig. 26). Moreover, Ifi27l2a and ISG15, two of the interferon-stimulated genes (ISGs), are identified as miRNA targets enriched in the RISC by Dicer in plaque macrophages, suggesting Dicer may also limit interferon response in plaque macrophages by directly targeting interferon-stimulated genes. Thus, these findings indicate that Dicer limits interferon signaling in LD^{high} macrophages through two distinct mechanisms—by restricting mtDNA release and directly suppressing ISG expression. Interferon signaling, triggered by pathogen- or self-derived nucleic acids, induces an antiviral state by promoting inflammation, cell cycle arrest, and apoptosis sensitization. Although interferon response is crucial for antiviral defense, its aberrant activation under pathogen-free conditions by endogenous stimuli can cause excessive inflammation and cell death[75,108,109]. My observations suggest that Dicer may protect against LD^{high} macrophage damage caused by interferon signaling activation.

Notably, LPS/IFN-γ treatment induces the activation of interferon signaling. This aligns with the previous study that LPS is a known interferon inducer, enhances type I interferon response by promoting IFN-β production[110]. However, in contrast to the effect on oxLDL-treated BMDMs, Dicer enhanced interferon signaling activation after LPS/IFN-γ treatment. This is probably due to Dicer-mediated production of miR-155[111], which is up-regulated after LPS/IFN-γ treatment in macrophages[112,113]. Previous studies have shown that miR-155 expression enhances interferon response by targeting SOCS1, a negative regulator of type I interferon signaling, in macrophages[114,115]. This suggests that Dicer may promote LPS/IFN-γ-induced interferon response by generating miR-155. Thus, distinct miRNA expression patterns in response to different stimuli shape Dicer's role in regulating interferon

signaling in opposing ways. Whereas Dicer suppresses interferon response triggered by self-derived nucleic acids in oxLDL-treated macrophages, it enhances the response induced by pathogen-related molecular patterns in LPS/IFN-γ-treated macrophages. In this way, Dicer facilitates the precise activation of interferon signaling to counteract pathogen-induced damage while preventing an overreaction to self-derived stimulation. However, further studies are needed to confirm this hypothesis.

4.6 Limitation

One limitation of this study is that the LysMCre/Dicer$^{flox/flox}$ genotype also induces a Dicer knockout in neutrophils, compromising the specificity of Dicer deletion in macrophages. However, since foam cells are primarily derived from macrophages rather than neutrophils, this model remains specific for studying the role of LD^{high} macrophages in plaques. Moreover, the ex vivo live plaque imaging was conducted under static conditions, which lack the physiological shear stress and hemodynamic forces present in vivo. This limitation may introduce slight deviations from the in vivo situation, particularly in processes sensitive to flow dynamics.

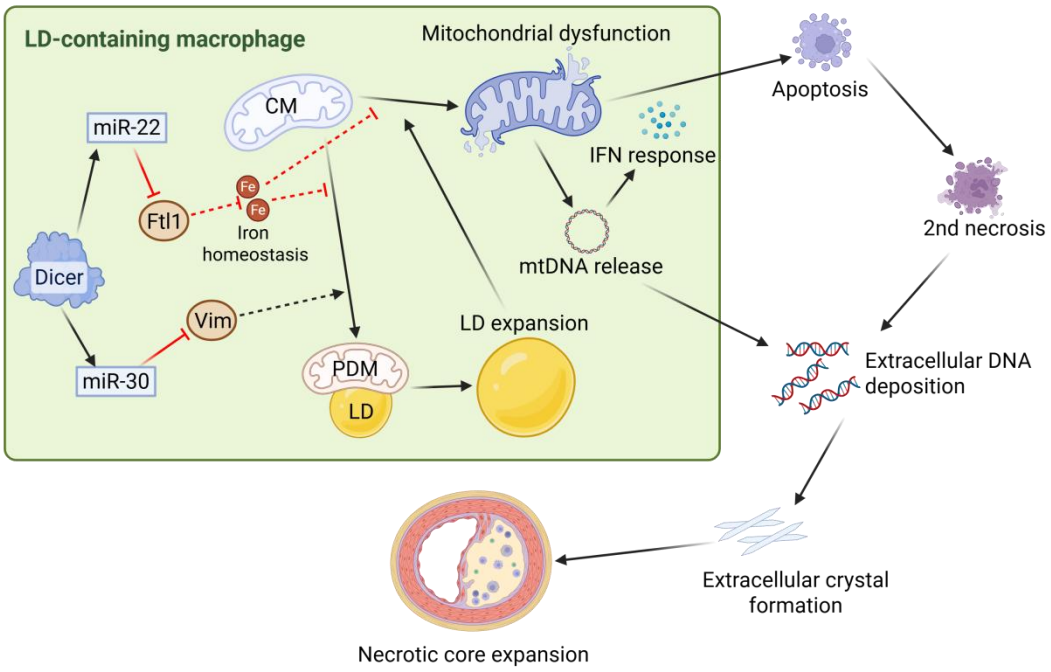

Fig. 26: Graphic summary. Dicer maintains mitochondrial homeostasis in LD-containing macrophages and limits CC-driven necrotic core expansion in atherosclerosis

In atherosclerotic plaques, Dicer expression in macrophages limits PDM formation and LD expansion, preserving mitochondrial integrity. Mitochondrial dysfunction in the absence of Dicer leads to mtDNA release, type I interferon activation, and secondary necrosis. The resulting extracellular DNA promotes CC formation, contributing to necrotic core expansion and plaque progression. Thus, Dicer protects against atherogenesis by maintaining metabolic and structural balance in plaque macrophages. This protective effect may involve the Dicer-regulated miR-22-Ftl1 and miR-30-Vim axes, which have been implicated in regulating mitochondrial function through iron homeostasis and cytoskeletal remodeling, respectively.

Summary

Necrotic core expansion is a critical determinant of plaque vulnerability in atherosclerosis, as it increases the risk of plaque rupture and subsequent thrombotic complications, such as myocardial infarction and stroke. CC formation is one of the key drivers of necrotic core formation. Although CC formation within the plaque has been attributed to the secondary necrosis of plaque macrophages and the accumulation of free cholesterol, the underlying mechanisms remain incompletely understood. Our previous study demonstrated that Dicer expression in macrophages limits plaque macrophage apoptosis and necrotic core formation in atherosclerosis. In vitro, Dicer promotes mitochondrial respiration in LD-containing macrophages. Based on this, this study hypothesizes that Dicer limits apoptosis and secondary necrosis of LD-containing plaque macrophages by enhancing mitochondrial respiration, thus restricting CC formation and subsequent necrotic core expansion.

To test this hypothesis, I established a live-plaque confocal imaging protocol using live plaque tissue from mTmG reporter mice to investigate the role of Dicer in regulating mitochondrial function and secondary necrosis of LD-containing plaque macrophages under real-time and 3D structural conditions. Additionally, I assessed the mitochondrial respiration of plaque cells using the Seahorse assay with live plaque tissue. Moreover, I combined the live plaque imaging with reflection confocal microscopy to investigate how secondary necrosis of plaque macrophages contributes to CC formation. To elucidate the mechanism through which miRNAs mediate the effects of Dicer on plaque macrophages, I performed integrated multi-omics analysis, including GFP-RIP-seq of the aorta and BMDMs from tAGO2 mice, along with proteomics and NanoString microRNA profiling of LD-containing BMDMs.

In this study, three plaque macrophage subtypes were identified according to LD content: LD^{high}, LD^{inter}, and LD^{low} macrophages. Notably, LD accumulation in the LD^{high} macrophages is associated with reduced mitochondrial activity. This is confirmed by the reduction of oxygen consumption in atherosclerotic plaques because of a mitochondrial proton leak in macrophages. The expression of Dicer in macrophages limits LD expansion by reducing PDM abundance during the transformation of LD^{inter} cells to LD^{high} macrophages, thus reducing the number of LD^{high} macrophages in the plaque.

Furthermore, Dicer-mediated enhancement of mitochondrial activity in LDhigh macrophages correlated with decreased caspase 3 activation, implying that Dicer may inhibit intrinsic apoptosis triggered by mitochondrial dysfunction. Additionally,

Dicer limited cytosolic DNA distribution, likely mtDNA, in LD^{high} macrophages by preventing mitochondrial dysfunction. This is confirmed in LD-containing BMDMs, where Dicer reduced mtDNA release and subsequent activation of the type I interferon response. Additionally, Dicer decreased secondary necrosis of LD^{high} macrophages, indicated by reduced extracellular deposition of apoptotic DNA , and CC formation in the plaque. Because crystals formed close to extracellular apoptotic DNA, extracellular DNA may facilitate CC formation. Thus, the effect of Dicer on the secondary necrosis of LD^{high} macropages may inhibit CC formation. Collectively, this study uncovers a critical role for Dicer in limiting CC formation in the necrotic core by preventing mitochondrial dysfunction and LD accumulation in LD^{high} macrophages, thereby restraining secondary necrosis and subsequent extracellular DNA deposition. Multi-omics analysis indicated that miR-22-mediated targeting of Ftl1, which regulates intracellular iron homeostasis, plays a crucial role in Dicer's effect on LD formation and necrotic core expansion, probably by preserving mitochondrial function.

These findings provide novel insights into the regulation of CC formation. Dicer and miR22, by regulating Ftl1 expression in plaque LD^{high} macrophages, may serve as potential therapeutic targets for preventing atherosclerotic progression, particularly CC-associated necrotic core expansion. Nevertheless, further investigation is needed to reveal how Ftl-1-mediated iron homeostasis regulates the function of LD^{high} macrophages, CC formation, and necrotic core formation.

References

1 Martin, S. S. *et al.* 2024 Heart Disease and Stroke Statistics: A Report of US and Global Data From the American Heart Association. *Circulation* **149**, e347-e913 (2024). https://doi.org/10.1161/CIR.0000000000001209

2 Libby, P. The changing landscape of atherosclerosis. *Nature* **592**, 524-533 (2021). https://doi.org/10.1038/s41586-021-03392-8

3 Shantsila, A. *et al.* Persistent macrovascular and microvascular dysfunction in patients with malignant hypertension. *Hypertension* **57**, 490-496 (2011). https://doi.org/10.1161/HYPERTENSIONAHA.110.166314

4 Bornfeldt, K. E. & Tabas, I. Insulin resistance, hyperglycemia, and atherosclerosis. *Cell Metab* **14**, 575-585 (2011). https://doi.org/10.1016/j.cmet.2011.07.015

5 Souilhol, C. *et al.* Endothelial responses to shear stress in atherosclerosis: a novel role for developmental genes. *Nat Rev Cardiol* **17**, 52-63 (2020). https://doi.org/10.1038/s41569-019-0239-5

6 Syvaranta, S. *et al.* Potential pathological roles for oxidized low-density lipoprotein and scavenger receptors SR-AI, CD36, and LOX-1 in aortic valve stenosis. *Atherosclerosis* **235**, 398-407 (2014). https://doi.org/10.1016/j.atherosclerosis.2014.05.933

7 Bowden, K. L. *et al.* LAL (Lysosomal Acid Lipase) Promotes Reverse Cholesterol Transport In Vitro and In Vivo. *Arterioscler Thromb Vasc Biol* **38**, 1191-1201 (2018). https://doi.org/10.1161/ATVBAHA.117.310507

8 Chistiakov, D. A., Bobryshev, Y. V. & Orekhov, A. N. Macrophage-mediated cholesterol handling in atherosclerosis. *J Cell Mol Med* **20**, 17-28 (2016). https://doi.org/10.1111/jcmm.12689

9 Ghosh, S., Zhao, B., Bie, J. & Song, J. Macrophage cholesteryl ester mobilization and atherosclerosis. *Vascul Pharmacol* **52**, 1-10 (2010). https://doi.org/10.1016/j.vph.2009.10.002

10 Vergallo, R. & Crea, F. Atherosclerotic Plaque Healing. *N Engl J Med* **383**, 846-857 (2020). https://doi.org/10.1056/NEJMra2000317

11 Tabas, I. Free cholesterol-induced cytotoxicity a possible contributing factor to macrophage foam cell necrosis in advanced atherosclerotic lesions. *Trends Cardiovasc Med* **7**, 256-263 (1997). https://doi.org/10.1016/S1050-1738(97)00086-8

12 Tabas, I. Consequences of cellular cholesterol accumulation: basic concepts and physiological implications. *J Clin Invest* **110**, 905-911 (2002). https://doi.org/10.1172/JCI16452

13 Devries-Seimon, T. *et al.* Cholesterol-induced macrophage apoptosis requires ER stress pathways and engagement of the type A scavenger receptor. *J Cell Biol* **171**, 61-73 (2005). https://doi.org/10.1083/jcb.200502078

14 Yao, P. M. & Tabas, I. Free cholesterol loading of macrophages is associated with widespread mitochondrial dysfunction and activation of the mitochondrial apoptosis pathway. *J Biol Chem* **276**, 42468-42476 (2001). https://doi.org/10.1074/jbc.M101419200

15 Bjorkhem, I. Do oxysterols control cholesterol homeostasis? *J Clin Invest* **110**, 725-730 (2002). https://doi.org/10.1172/JCI16388

16 Libby, P. *et al.* Atherosclerosis. *Nat Rev Dis Primers* **5**, 56 (2019). https://doi.org/10.1038/s41572-019-0106-z

17 Badimon, L. & Vilahur, G. Thrombosis formation on atherosclerotic lesions and plaque rupture. *J Intern Med* **276**, 618-632 (2014). https://doi.org/10.1111/joim.12296

18 Xu, M. *et al.* Effects of mitochondrial dysfunction on cellular function: Role in atherosclerosis. *Biomed Pharmacother* **174**, 116587 (2024). https://doi.org/10.1016/j.biopha.2024.116587

19 Madamanchi, N. R. & Runge, M. S. Mitochondrial dysfunction in atherosclerosis. *Circ Res* **100**, 460-473 (2007). https://doi.org/10.1161/01.RES.0000258450.44413.96

20 Ren, J., Bi, Y., Sowers, J. R., Hetz, C. & Zhang, Y. Endoplasmic reticulum stress and unfolded protein response in cardiovascular diseases. *Nat Rev Cardiol* **18**, 499-521 (2021). https://doi.org/10.1038/s41569-021-00511-w

21 Liu, C., Jiang, Z., Pan, Z. & Yang, L. The Function, Regulation and Mechanism of Programmed Cell Death of Macrophages in Atherosclerosis. *Front Cell Dev Biol* **9**, 809516 (2021). https://doi.org/10.3389/fcell.2021.809516

22 Tabas, I. Macrophage death and defective inflammation resolution in atherosclerosis. *Nat Rev Immunol* **10**, 36-46 (2010). https://doi.org/10.1038/nri2675

23 Back, M., Yurdagul, A., Jr., Tabas, I., Oorni, K. & Kovanen, P. T. Inflammation and its resolution in atherosclerosis: mediators and therapeutic opportunities. *Nat Rev Cardiol* **16**, 389-406 (2019). https://doi.org/10.1038/s41569-019-0169-2

24 Schober, A. *et al.* MicroRNA-21 Controls Circadian Regulation of Apoptosis in Atherosclerotic Lesions. *Circulation* **144**, 1059-1073 (2021). https://doi.org/10.1161/CIRCULATIONAHA.120.051614

25 Baumer, Y., Mehta, N. N., Dey, A. K., Powell-Wiley, T. M. & Boisvert, W. A. Cholesterol crystals and atherosclerosis. *Eur Heart J* **41**, 2236-2239 (2020). https://doi.org/10.1093/eurheartj/ehaa505

26 Baumer, Y., Irei, J. & Boisvert, W. A. Cholesterol crystals in the pathogenesis of atherosclerosis. *Nat Rev Cardiol* (2024). https://doi.org/10.1038/s41569-024-01100-3

27 Vedre, A. *et al.* Physical factors that trigger cholesterol crystallization leading to plaque rupture. *Atherosclerosis* **203**, 89-96 (2009). https://doi.org/10.1016/j.atherosclerosis.2008.06.027

28 Janoudi, A., Shamoun, F. E., Kalavakunta, J. K. & Abela, G. S. Cholesterol crystal induced arterial inflammation and destabilization of atherosclerotic plaque. *Eur Heart J* **37**, 1959-1967 (2016). https://doi.org/10.1093/eurheartj/ehv653

29 Abela, G. S. & Aziz, K. Cholesterol crystals rupture biological membranes and human plaques during acute cardiovascular events--a novel insight into plaque rupture by scanning electron microscopy. *Scanning* **28**, 1-10 (2006). https://doi.org/10.1002/sca.4950280101

30 Tabas, I. & Bornfeldt, K. E. Macrophage Phenotype and Function in Different Stages of Atherosclerosis. *Circ Res* **118**, 653-667 (2016). https://doi.org/10.1161/CIRCRESAHA.115.306256

31 Frostegard, J. *et al.* Cytokine expression in advanced human atherosclerotic plaques: dominance of pro-inflammatory (Th1) and macrophage-stimulating cytokines. *Atherosclerosis* **145**, 33-43 (1999). https://doi.org/10.1016/s0021-9150(99)00011-8

32 Jinnouchi, H. *et al.* Diversity of macrophage phenotypes and responses in atherosclerosis. *Cell Mol Life Sci* **77**, 1919-1932 (2020). https://doi.org/10.1007/s00018-019-03371-3

33 Koelwyn, G. J., Corr, E. M., Erbay, E. & Moore, K. J. Regulation of macrophage immunometabolism in atherosclerosis. *Nat Immunol* **19**, 526-537 (2018). https://doi.org/10.1038/s41590-018-0113-3

34 Vallejo, J., Cochain, C., Zernecke, A. & Ley, K. Heterogeneity of immune cells in human atherosclerosis revealed by scRNA-Seq. *Cardiovasc Res* **117**, 2537-2543 (2021). https://doi.org/10.1093/cvr/cvab260

35 Williams, J. W. *et al.* Limited proliferation capacity of aortic intima resident macrophages requires monocyte recruitment for atherosclerotic plaque progression. *Nat Immunol* **21**, 1194-1204 (2020). https://doi.org/10.1038/s41590-020-0768-4

36 Zernecke, A. *et al.* Integrated single-cell analysis-based classification of vascular mononuclear phagocytes in mouse and human atherosclerosis. *Cardiovasc Res* **119**, 1676-1689 (2023). https://doi.org/10.1093/cvr/cvac161

37 Willemsen, L. & de Winther, M. P. Macrophage subsets in atherosclerosis as defined by single-cell technologies. *J Pathol* **250**, 705-714 (2020). https://doi.org/10.1002/path.5392

38 Cochain, C. *et al.* Single-Cell RNA-Seq Reveals the Transcriptional Landscape and Heterogeneity of Aortic Macrophages in Murine Atherosclerosis. *Circ Res* **122**, 1661-1674 (2018). https://doi.org/10.1161/CIRCRESAHA.117.312509

39 Winkels, H. *et al.* Atlas of the Immune Cell Repertoire in Mouse Atherosclerosis Defined by Single-Cell RNA-Sequencing and Mass Cytometry. *Circ Res* **122**, 1675-1688 (2018). https://doi.org/10.1161/CIRCRESAHA.117.312513

40 Depuydt, M. A. C. *et al.* Microanatomy of the Human Atherosclerotic Plaque by Single-Cell Transcriptomics. *Circ Res* **127**, 1437-1455 (2020). https://doi.org/10.1161/CIRCRESAHA.120.316770

41 Macrae, I. J. *et al.* Structural basis for double-stranded RNA processing by Dicer. *Science* **311**, 195-198 (2006). https://doi.org/10.1126/science.1121638

42 Tian, Y. *et al.* A phosphate-binding pocket within the platform-PAZ-connector helix cassette of human Dicer. *Mol Cell* **53**, 606-616 (2014). https://doi.org/10.1016/j.molcel.2014.01.003

43 Lau, P. W. *et al.* The molecular architecture of human Dicer. *Nat Struct Mol Biol* **19**, 436-440 (2012). https://doi.org/10.1038/nsmb.2268

44 Lau, P. W., Potter, C. S., Carragher, B. & MacRae, I. J. Structure of the human Dicer-TRBP complex by electron microscopy. *Structure* **17**, 1326-1332 (2009). https://doi.org/10.1016/j.str.2009.08.013

45 Liu, Z. *et al.* Cryo-EM Structure of Human Dicer and Its Complexes with a Pre-miRNA Substrate. *Cell* **173**, 1549-1550 (2018). https://doi.org/10.1016/j.cell.2018.05.031

46 Zhang, H., Kolb, F. A., Jaskiewicz, L., Westhof, E. & Filipowicz, W. Single processing center models for human Dicer and bacterial RNase III. *Cell* **118**, 57-68 (2004). https://doi.org/10.1016/j.cell.2004.06.017

47 Schober, A. & Weber, C. Mechanisms of MicroRNAs in Atherosclerosis. *Annu Rev Pathol* **11**, 583-616 (2016). https://doi.org/10.1146/annurev-pathol-012615-044135

48 Ciechanowska, K., Pokornowska, M. & Kurzynska-Kokorniak, A. Genetic Insight into the Domain Structure and Functions of Dicer-Type Ribonucleases. *Int J Mol Sci* **22** (2021). https://doi.org/10.3390/ijms22020616

49 Iwasaki, S. *et al.* Hsc70/Hsp90 chaperone machinery mediates ATP-dependent RISC loading of small RNA duplexes. *Mol Cell* **39**, 292-299 (2010). https://doi.org/10.1016/j.molcel.2010.05.015

50 Miyoshi, K., Miyoshi, T., Hartig, J. V., Siomi, H. & Siomi, M. C. Molecular mechanisms that funnel RNA precursors into endogenous small-interfering RNA and microRNA biogenesis pathways in Drosophila. *RNA* **16**, 506-515 (2010). https://doi.org/10.1261/rna.1952110

51 Meister, G. Argonaute proteins: functional insights and emerging roles. *Nat Rev Genet* **14**, 447-459 (2013). https://doi.org/10.1038/nrg3462

52 Bartel, D. P. MicroRNAs: target recognition and regulatory functions. *Cell* **136**, 215-233 (2009). https://doi.org/10.1016/j.cell.2009.01.002

53 Jonas, S. & Izaurralde, E. Towards a molecular understanding of microRNA-mediated gene silencing. *Nat Rev Genet* **16**, 421-433 (2015). https://doi.org/10.1038/nrg3965

54 Iwakawa, H. O. & Tomari, Y. Life of RISC: Formation, action, and degradation of RNA-induced silencing complex. *Mol Cell* **82**, 30-43 (2022). https://doi.org/10.1016/j.molcel.2021.11.026

55 Buhler, M., Verdel, A. & Moazed, D. Tethering RITS to a nascent transcript initiates RNAi- and heterochromatin-dependent gene silencing. *Cell* **125**, 873-886 (2006). https://doi.org/10.1016/j.cell.2006.04.025

56 Gao, Z. *et al.* An RNA polymerase II- and AGO4-associated protein acts in RNA-directed DNA methylation. *Nature* **465**, 106-109 (2010). https://doi.org/10.1038/nature09025

57 Place, R. F., Li, L. C., Pookot, D., Noonan, E. J. & Dahiya, R. MicroRNA-373 induces expression of genes with complementary promoter sequences. *Proc Natl Acad Sci U S A* **105**, 1608-1613 (2008). https://doi.org/10.1073/pnas.0707594105

58 Francia, S. *et al.* Site-specific DICER and DROSHA RNA products control the DNA-damage response. *Nature* **488**, 231-235 (2012). https://doi.org/10.1038/nature11179

59 White, E., Schlackow, M., Kamieniarz-Gdula, K., Proudfoot, N. J. & Gullerova, M. Human nuclear Dicer restricts the deleterious accumulation of endogenous double-stranded RNA. *Nat Struct Mol Biol* **21**, 552-559 (2014). https://doi.org/10.1038/nsmb.2827

60 Schober, A., Nazari-Jahantigh, M. & Weber, C. MicroRNA-mediated mechanisms of the cellular stress response in atherosclerosis. *Nat Rev Cardiol* **13**, 120 (2016). https://doi.org/10.1038/nrcardio.2015.190

61 Ouimet, M. *et al.* microRNA-33 Regulates Macrophage Autophagy in Atherosclerosis. *Arterioscler Thromb Vasc Biol* **37**, 1058-1067 (2017). https://doi.org/10.1161/ATVBAHA.116.308916

62 Tian, F. J. *et al.* Elevated microRNA-155 promotes foam cell formation by targeting HBP1 in atherogenesis. *Cardiovasc Res* **103**, 100-110 (2014). https://doi.org/10.1093/cvr/cvu070

63 Wei, Y. *et al.* The microRNA-342-5p fosters inflammatory macrophage activation through an Akt1- and microRNA-155-dependent pathway during atherosclerosis. *Circulation* **127**, 1609-1619 (2013). https://doi.org/10.1161/CIRCULATIONAHA.112.000736

64 Karshovska, E. *et al.* HIF-1alpha (Hypoxia-Inducible Factor-1alpha) Promotes Macrophage Necroptosis by Regulating miR-210 and miR-383. *Arterioscler Thromb Vasc Biol* **40**, 583-596 (2020). https://doi.org/10.1161/ATVBAHA.119.313290

65 Wei, Y. *et al.* Dicer in Macrophages Prevents Atherosclerosis by Promoting Mitochondrial Oxidative Metabolism. *Circulation* **138**, 2007-2020 (2018). https://doi.org/10.1161/CIRCULATIONAHA.117.031589

66 Bernstein, E. *et al.* Dicer is essential for mouse development. *Nat Genet* **35**, 215-217 (2003). https://doi.org/10.1038/ng1253

67 Hartmann, P. *et al.* Endothelial Dicer promotes atherosclerosis and vascular inflammation by miRNA-103-mediated suppression of KLF4. *Nat Commun* **7**, 10521 (2016). https://doi.org/10.1038/ncomms10521

68 Harfe, B. D., McManus, M. T., Mansfield, J. H., Hornstein, E. & Tabin, C. J. The RNaseIII enzyme Dicer is required for morphogenesis but not patterning of the vertebrate limb. *Proc Natl Acad Sci U S A* **102**, 10898-10903 (2005). https://doi.org/10.1073/pnas.0504834102

69 Muzumdar, M. D., Tasic, B., Miyamichi, K., Li, L. & Luo, L. A global double-fluorescent Cre reporter mouse. *Genesis* **45**, 593-605 (2007). https://doi.org/10.1002/dvg.20335

70 He, M. *et al.* Cell-type-based analysis of microRNA profiles in the mouse brain. *Neuron* **73**, 35-48 (2012). https://doi.org/10.1016/j.neuron.2011.11.010

71 Kaseder, M. *et al.* Evidence of a role for cAMP in mitochondrial regulation in ovarian granulosa cells. *Mol Hum Reprod* **28** (2022). https://doi.org/10.1093/molehr/gaac030

72 Janjic, A. *et al.* Prime-seq, efficient and powerful bulk RNA sequencing. *Genome Biol* **23**, 88 (2022). https://doi.org/10.1186/s13059-022-02660-8

73 Benador, I. Y., Veliova, M., Liesa, M. & Shirihai, O. S. Mitochondria Bound to Lipid Droplets: Where Mitochondrial Dynamics Regulate Lipid Storage and Utilization. *Cell Metab* **29**, 827-835 (2019). https://doi.org/10.1016/j.cmet.2019.02.011

74 Benador, I. Y. *et al.* Mitochondria Bound to Lipid Droplets Have Unique Bioenergetics, Composition, and Dynamics that Support Lipid Droplet Expansion. *Cell Metab* **27**, 869-885 e866 (2018). https://doi.org/10.1016/j.cmet.2018.03.003

75 Hu, M. M. & Shu, H. B. Mitochondrial DNA-triggered innate immune response: mechanisms and diseases. *Cell Mol Immunol* **20**, 1403-1412 (2023). https://doi.org/10.1038/s41423-023-01086-x

76 West, A. P. *et al.* Mitochondrial DNA stress primes the antiviral innate immune response. *Nature* **520**, 553-557 (2015). https://doi.org/10.1038/nature14156

77 Yu, J. *et al.* Lipid droplet remodeling and interaction with mitochondria in mouse brown adipose tissue during cold treatment. *Biochim Biophys Acta* **1853**, 918-928 (2015). https://doi.org/10.1016/j.bbamcr.2015.01.020

78 Wang, H. *et al.* Cardiomyocyte-specific perilipin 5 overexpression leads to myocardial steatosis and modest cardiac dysfunction. *J Lipid Res* **54**, 953-965 (2013). https://doi.org/10.1194/jlr.M032466

79 Wang, H. *et al.* Perilipin 5, a lipid droplet-associated protein, provides physical and metabolic linkage to mitochondria. *J Lipid Res* **52**, 2159-2168 (2011). https://doi.org/10.1194/jlr.M017939

80 Tarnopolsky, M. A. *et al.* Influence of endurance exercise training and sex on intramyocellular lipid and mitochondrial ultrastructure, substrate use, and mitochondrial enzyme activity. *Am J Physiol Regul Integr Comp Physiol* **292**, R1271-1278 (2007). https://doi.org/10.1152/ajpregu.00472.2006

81 Tarique, I. *et al.* LIPOPHAGY: a novel form of steroidogenic activity within the LEYDIG cell during the reproductive cycle of turtle. *Reprod Biol Endocrinol* **17**, 19 (2019). https://doi.org/10.1186/s12958-019-0462-2

82 Hall, P. F. The roles of calmodulin, actin, and vimentin in steroid synthesis by adrenal cells. *Steroids* **62**, 185-189 (1997). https://doi.org/10.1016/s0039-128x(96)00179-1

83 Robichaud, S. *et al.* Identification of novel lipid droplet factors that regulate lipophagy and cholesterol efflux in macrophage foam cells. *Autophagy* **17**, 3671-3689 (2021). https://doi.org/10.1080/15548627.2021.1886839

84 Shi, S. *et al.* Podocyte-selective deletion of dicer induces proteinuria and glomerulosclerosis. *J Am Soc Nephrol* **19**, 2159-2169 (2008). https://doi.org/10.1681/ASN.2008030312

85 Gupta, P., Singh, P., Pandey, H. S., Seth, P. & Mukhopadhyay, C. K. Phosphoinositide-3-kinase inhibition elevates ferritin level resulting depletion of labile iron pool and blocking of glioma cell proliferation. *Biochim Biophys Acta Gen Subj* **1863**, 547-564 (2019). https://doi.org/10.1016/j.bbagen.2018.12.013

86 Long, M. *et al.* DGAT1 activity synchronises with mitophagy to protect cells from metabolic rewiring by iron depletion. *EMBO J* **41**, e109390 (2022). https://doi.org/10.15252/embj.2021109390

87 Wolk, M. & Fedorova, M. The lipid droplet lipidome. *FEBS Lett* **598**, 1215-1225 (2024). https://doi.org/10.1002/1873-3468.14874

88 Xiong, J. *et al.* Bulk and single-cell characterisation of the immune heterogeneity of atherosclerosis identifies novel targets for immunotherapy. *BMC Biol* **21**, 46 (2023). https://doi.org/10.1186/s12915-023-01540-2

89 Aflaki, E. *et al.* Triacylglycerol accumulation activates the mitochondrial apoptosis pathway in macrophages. *J Biol Chem* **286**, 7418-7428 (2011). https://doi.org/10.1074/jbc.M110.175703

90 Gordan, R. *et al.* Involvement of cytosolic and mitochondrial iron in iron overload cardiomyopathy: an update. *Heart Fail Rev* **23**, 801-816 (2018). https://doi.org/10.1007/s10741-018-9700-5

91 Zhang, H. *et al.* Myocardial Iron Deficiency and Mitochondrial Dysfunction in Advanced Heart Failure in Humans. *J Am Heart Assoc* **11**, e022853 (2022). https://doi.org/10.1161/JAHA.121.022853

92 Sawicki, K. T., De Jesus, A. & Ardehali, H. Iron Metabolism in Cardiovascular Disease: Physiology, Mechanisms, and Therapeutic Targets. *Circ Res* **132**, 379-396 (2023). https://doi.org/10.1161/CIRCRESAHA.122.321667

93 Glover, H. L., Schreiner, A., Dewson, G. & Tait, S. W. G. Mitochondria and cell death. *Nat Cell Biol* **26**, 1434-1446 (2024). https://doi.org/10.1038/s41556-024-01429-4

94 Puylaert, P., Zurek, M., Rayner, K. J., De Meyer, G. R. Y. & Martinet, W. Regulated Necrosis in Atherosclerosis. *Arterioscler Thromb Vasc Biol* **42**, 1283-1306 (2022). https://doi.org/10.1161/ATVBAHA.122.318177

95 Shi, C. *et al.* Crystal Clots as Therapeutic Target in Cholesterol Crystal Embolism. *Circ Res* **126**, e37-e52 (2020). https://doi.org/10.1161/CIRCRESAHA.119.315625

96 Wang, H. H., Portincasa, P., Liu, M. & Wang, D. Q. Effects of Biliary Phospholipids on Cholesterol Crystallization and Growth in Gallstone Formation. *Adv Ther* **40**, 743-768 (2023). https://doi.org/10.1007/s12325-022-02407-8

97 Lee, H. R., Kang, S. & Choi, S. Q. Lipid Droplet Surface Promotes 3D Morphological Evolution of Non-Rhomboidal Cholesterol Crystals. *Adv Sci (Weinh)* **12**, e2409201 (2025). https://doi.org/10.1002/advs.202409201

98 Gao, Q. *et al.* Halide Perovskite Crystallization Processes and Methods in Nanocrystals, Single Crystals, and Thin Films. *Adv Mater* **34**, e2200720 (2022). https://doi.org/10.1002/adma.202200720

99 Varsano, N. *et al.* Two polymorphic cholesterol monohydrate crystal structures form in macrophage culture models of atherosclerosis. *Proc Natl Acad Sci U S A* **115**, 7662-7669 (2018). https://doi.org/10.1073/pnas.1803119115

100 Capua-Shenkar, J. *et al.* Examining atherosclerotic lesions in three dimensions at the nanometer scale with cryo-FIB-SEM. *Proc Natl Acad Sci U S A* **119**, e2205475119 (2022). https://doi.org/10.1073/pnas.2205475119

101 Cabrera-Reyes, F., Parra-Ruiz, C., Yuseff, M. I. & Zanlungo, S. Alterations in Lysosome Homeostasis in Lipid-Related Disorders: Impact on Metabolic Tissues and Immune Cells. *Front Cell Dev Biol* **9**, 790568 (2021). https://doi.org/10.3389/fcell.2021.790568

102 Cantuti-Castelvetri, L. *et al.* Defective cholesterol clearance limits remyelination in the aged central nervous system. *Science* **359**, 684-688 (2018). https://doi.org/10.1126/science.aan4183

103 Duewell, P. *et al.* NLRP3 inflammasomes are required for atherogenesis and activated by cholesterol crystals. *Nature* **464**, 1357-1361 (2010). https://doi.org/10.1038/nature08938

104 He, X. *et al.* Pyroptosis is a critical immune-inflammatory response involved in atherosclerosis. *Pharmacol Res* **165**, 105447 (2021). https://doi.org/10.1016/j.phrs.2021.105447

105 Shi, Q. *et al.* Increased glucose metabolism in TAMs fuels O-GlcNAcylation of lysosomal Cathepsin B to promote cancer metastasis and chemoresistance. *Cancer Cell* **40**, 1207-1222 e1210 (2022). https://doi.org/10.1016/j.ccell.2022.08.012

106 Sendler, M. *et al.* Cathepsin B Activity Initiates Apoptosis via Digestive Protease Activation in Pancreatic Acinar Cells and Experimental Pancreatitis. *J Biol Chem* **291**, 14717-14731 (2016). https://doi.org/10.1074/jbc.M116.718999

107 Hu, Y. *et al.* Blockade of Autophagy Prevents the Progression of Hyperuricemic Nephropathy Through Inhibiting NLRP3 Inflammasome-Mediated Pyroptosis. *Front Immunol* **13**, 858494 (2022). https://doi.org/10.3389/fimmu.2022.858494

108 Kretschmer, S. & Lee-Kirsch, M. A. Type I interferon-mediated autoinflammation and autoimmunity. *Curr Opin Immunol* **49**, 96-102 (2017). https://doi.org/10.1016/j.coi.2017.09.003

109 Takeuchi, O. & Akira, S. Pattern recognition receptors and inflammation. *Cell* **140**, 805-820 (2010). https://doi.org/10.1016/j.cell.2010.01.022

110 Pulverer, J. E. *et al.* Temporal and spatial resolution of type I and III interferon responses in vivo. *J Virol* **84**, 8626-8638 (2010). https://doi.org/10.1128/JVI.00303-10

111 Yao, M. *et al.* Dicer mediating the expression of miR-143 and miR-155 regulates hexokinase II associated cellular response to hypoxia. *Am J Physiol Lung Cell Mol Physiol* **307**, L829-837 (2014). https://doi.org/10.1152/ajplung.00081.2014

112 Bruen, R., Fitzsimons, S. & Belton, O. miR-155 in the Resolution of Atherosclerosis. *Front Pharmacol* **10**, 463 (2019). https://doi.org/10.3389/fphar.2019.00463

113 Nazari-Jahantigh, M. *et al.* MicroRNA-155 promotes atherosclerosis by repressing Bcl6 in macrophages. *J Clin Invest* **122**, 4190-4202 (2012). https://doi.org/10.1172/JCI61716

114 Jafarzadeh, A. *et al.* MicroRNA-155 and antiviral immune responses. *Int Immunopharmacol* **101**, 108188 (2021). https://doi.org/10.1016/j.intimp.2021.108188

115 Wang, P. *et al.* Inducible microRNA-155 feedback promotes type I IFN signaling in antiviral innate immunity by targeting suppressor of cytokine signaling 1. *J Immunol* **185**, 6226-6233 (2010). https://doi.org/10.4049/jimmunol.1000491

Acknowledgements

I would like to take this opportunity to express my sincere gratitude to all those who supported me throughout my doctoral studies.

First and foremost, I am deeply grateful to my supervisor, Prof. Dr. Andreas Schober, whose insightful academic guidance, constructive feedback, and continuous support have been instrumental throughout my doctoral studies. His scientific expertise, critical perspective, and dedication to research have profoundly influenced my academic development and personal growth. I have greatly benefited from his mentorship, particularly the freedom and trust he offered me throughout my research, and working with him has been an enriching and enjoyable experience.

I would also like to thank the other members of my Thesis Advisory Committee, Prof.Dr. Christian Schulz and Prof.Dr. Sebastian Kobold, for their thoughtful feedback, constructive suggestions, and ongoing support in my research. Their guidance and critical suggestions during the meetings were instrumental in shaping the direction of this work.

I would also like to express my sincere gratitude to Dr. Maliheh Nazari Jahantigh for her generous support, patient guidance, and insightful scientific advice throughout my doctoral project. Her deep expertise and openness to discussion were of great value to me.

I would like to sincerely thank all my colleagues in our research group, including Claudia Geissler, Tanya Guduru, Khadijeh Taherdangkoo, Yanyi Zhou, Qiuxing Meng, and Shilun Li, for their support, helpful discussions, and the friendly atmosphere during my doctoral work. Working with such dedicated and knowledgeable teammates made this experience both productive and enjoyable. I am especially grateful for their openness and willingness to share ideas and provide assistance whenever needed.

I would also like to acknowledge the members of our collaborating groups, including Remco T.A. Megens, Prof. Dr. Alexander Bartelt, and Carolin Muley from IPEK, Prof. Dr. Axel Imhof and Ignasi Forné from ZfP of LMU, and Prof. Dr. Wolfgang Enard from the Anthropology & Human Genomics department of LMU, for their valuable contributions, scientific input, and technical support, which significantly enriched this project.

I thank the Institute for Cardiovascular Prevention (IPEK) and its director, Prof. Dr. med. Christian Weber, for providing an excellent research environment and continuous institutional support.

Additionally, I gratefully acknowledge the support from the Deutsche Forschungsgemeinschaft (German Research Foundation, Collaborative Research

Centre 1123) and the China Scholarship Council (CSC), both of which made this work possible.

Last, I would like to express my heartfelt gratitude to my family for their unwavering love, patience, and encouragement. Their support has been a constant source of strength throughout this journey.

Affidavit

Li, Nan

Surname, first name

I hereby declare, that the submitted thesis entitled:

The regulation of mitochondrial function and lipid droplet formation by Dicer in plaque macrophages

is my own work. I have only used the sources indicated and have not made unauthorised use of services of a third party. Where the work of others has been quoted or reproduced, the source is always given.

I further declare that the dissertation presented here has not been submitted in the same or similar form to any other institution for the purpose of obtaining an academic degree.

Munich, 21.12.2025

Place, Date

Nan Li

Signature doctoral candidate

LMU LUDWIG-MAXIMILIANS-UNIVERSITÄT MÜNCHEN

Dekanat Medizinische Fakultät
Promotionsbüro

Confirmation of congruency between printed and electronic version of the doctoral thesis

Li, Nan

Surname, first name

I hereby declare that the electronic version of the submitted thesis, entitled:

The regulation of mitochondrial function and lipid droplet formation by Dicer in plaque macrophages

is congruent with the printed version both in content and format.

Munich, 21.12.2025

Place, Date

Nan Li

Signature doctoral candidate